CHEMISTRY
A EUROPEAN JOURNAL

DOI: 10.1002/chem.200903381

Stabilization of High-Valent $Fe^{IV}S_6$-Cores by Dithiocarbamate(1−) and 1,2-Dithiolate(2−) Ligands in Octahedral $[Fe^{IV}(Et_2dtc)_{3-n}(mnt)_n]^{(n-1)-}$ Complexes ($n = 0, 1, 2, 3$): A Spectroscopic and Density Functional Theory Computational Study**

Carsten Milsmann,[a] Stephen Sproules,[a] Eckhard Bill,[a] Thomas Weyhermüller,[a] Serena DeBeer George,[b] and Karl Wieghardt*[a]

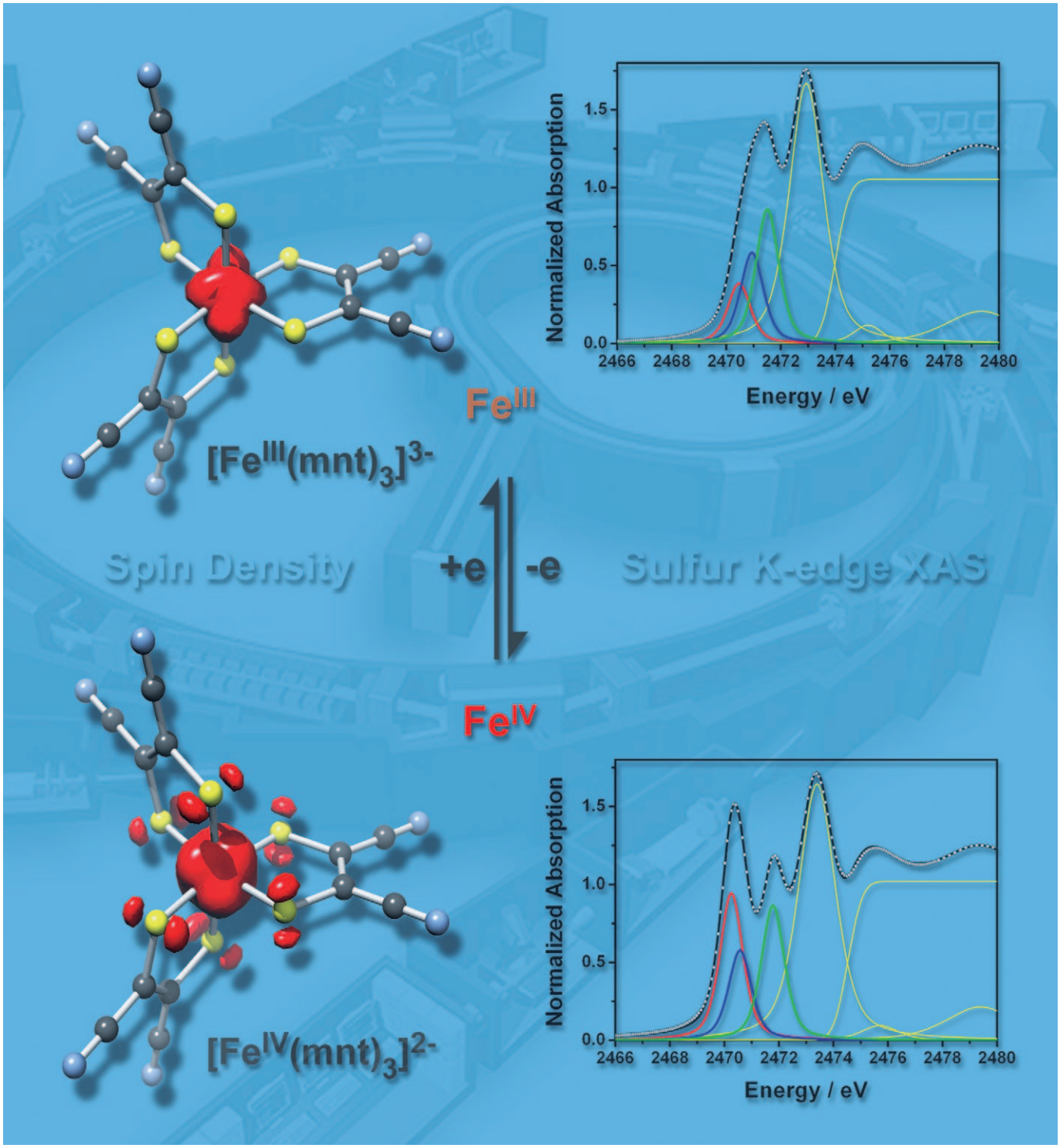

Abstract: A detailed spectroscopic and quantum chemical analysis is presented to elucidate the electronic structures of the octahedral complexes $[Fe(Et_2dtc)_{3-n}(mnt)_n]^{n-}$ (**1**–**4**, $n=3, 2, 1, 0$) and their one-electron oxidized analogues $[Fe(Et_2dtc)_{3-n}(mnt)_n]^{(n-1)-}$ (**1^{ox}**–**4^{ox}**); $(mnt)^{2-}$ represents maleonitriledithiolate(2−) and $(Et_2dtc)^{1-}$ is the diethyldithiocarbamato(1−) ligand. By using X-ray crystallography, Mössbauer spectroscopy, and Fe and S K-edge X-ray absorption spectroscopy (XAS) it is convincingly shown that, in contrast to our previous studies on [Fe(cyclam)(mnt)]$^{1+}$ (cyclam = 1,4,8,11-tetraazacyclotetradecane), the oxidation of **1**–**4** is metal-centered yielding the genuine Fe^{IV} complexes **1^{ox}**–**4^{ox}**. For the latter complexes, a spin ground state of $S=1$ has been established by magnetic susceptibility measurements, which indicates a low-spin d^4 configuration. DFT calculations at the B3LYP level support this electronic structure and exclude the presence of a ligand π radical coordinated to an intermediate-spin ferric ion. Mössbauer parameters and XAS spectra have been calculated to calibrate our computational results against the experiment. Finally, a simple ligand-field approach is presented to correlate the structural features obtained from X-ray crystallography (100 K) with the spectroscopic data.

Keywords: density functional calculations · dithiolenes · high-valent iron · S ligands · X-ray absorption spectroscopy

Introduction

Dithiocarbamato(1−) ligands are known to stabilize unusually high oxidation states (> +III) in their first-row transition metal-ion complexes. Thus, the monocations $[M^{IV}(S_2CNEt_2)_3]^+$ (M = Mn,[1–3] Fe,[2] Co,[3–5] Ni[6]) have been reported. In general, the MS_6 polyhedron is distorted octahedral and the observed electronic ground states are d^3 ($S=3/2$) for the Mn^{IV} complex, low-spin d^4 ($S=1$) for the Fe^{IV}, low-spin d^5 ($S=1/2$) for the Co^{IV}, and low-spin d^6 ($S=0$) for the Ni^{IV} analogue. It has convincingly been shown that the one-electron oxidation of diamagnetic $[Co^{III}(S_2CNEt_2)_3]$ to the corresponding monocation is metal-centered affording low-spin Co^{IV} ($S=1/2$).[4,5] EPR spectroscopy proved that the unpaired electron of $[Co^{IV}(S_2CNEt_2)_3]^+$ resides largely on the metal center confirming the unusual Co^{IV} oxidation state.[4] In no instance has an *S*,*S*′-coordinated dithiocarbamato(1−) ligand been shown to behave as a redox noninnocent ligand. The coordination chemistry of the hypothetical neutral radical $[S_2CNR_2]^{\bullet}$ has not been described to date.

It is now very interesting that the neutral $[Fe^{III}(S_2CNEt_2)_3]$ species[7] also undergoes a metal-centered one-electron oxidation affording the monocation $[Fe^{IV}(S_2CNEt_2)_3]^+$ ($S=1$) containing a low-spin Fe^{IV} ion (d^4).[2,8–11] The presence of high-valent Fe^{IV} has been deduced primarily from the fact that the isomer shifts of the neutral and the monocationic species differ by ~0.17 mm s^{-1}[12,13] and the observation that the C–N and C–S bond lengths of the *N*,*N*-diethyldithiocarbamate(1−) ligands in both structures are nearly identical (as are the average Fe–S bond lengths at 2.30 Å).

Maleonitriledithiolate(2−) (mnt^{2-}) is capable of forming the trianionic tris(dithiolate)iron(III) complex $[Fe(mnt)_3]^{3-}$ with an FeS_6-polyhedron and a low-spin central ferric ion.[14] The structure has not been reported, but its EPR and Mössbauer spectra have been recorded.[15,16] The corresponding dianion $[Fe(mnt)_3]^{2-}$ ($S=1$) has been synthesized and characterized by X-ray crystallography.[14,17–20] Again, based on the differing isomer shifts of the corresponding Mössbauer spectra of the tri- and dianion ($\Delta\delta = 0.14$ mm s^{-1}) it has been concluded[15,16] that the triplet dianion contains a low-spin Fe^{IV} ion (d^4, $S=1$). This implies that the one-electron oxidation from tri- to dianion is metal-centered and no $(mnt^{\bullet})^{1-}$ radical is involved.

On the other hand, we have recently shown[21] that the one-electron oxidation of $[Fe^{III}(cyclam)(mnt)]^+$ (cyclam = 1,4,8,11-tetraazacyclotetradecane; $S=1/2$) containing a low-spin ferric ion and a closed-shell $(mnt)^{2-}$ ligand yields the corresponding diamagnetic dication $[Fe^{III}(cyclam)(mnt^{\bullet})]^{2+}$ in which a low-spin ferric ion is intramolecularly antiferromagnetically coupled to a ligand π radical monoanion. Fe and S K-edge X-ray absorption spectroscopy (XAS) as well as Mössbauer spectroscopy and DFT calculations proved this electronic structure description unambiguously to be correct. No evidence for the presence of an Fe^{IV} ion in this dication was found. Interestingly, it has not been possible to convert the dication $[Fe(cyclam)(Et_2dtc)]^{2+}$ ($S=1/2$) to the corresponding trication. These experiments show that the $(mnt)^{2-}$ ligand is redox noninnocent, that is, the open-shell π radical oxidation level is in principle accessible. This appears not to be the case for closed-shell dithiocarbamate(1−) ligands.

Therefore, we decided to (re)investigate the complete series of complexes $[Fe(Et_2dtc)_{3-n}(mnt)_n]^{n-}$ (**1**–**4**, $n=3, 2, 1, 0$) shown in Scheme 1 and their corresponding one-electron

[a] Dr. C. Milsmann, Dr. S. Sproules, Dr. E. Bill, Dr. T. Weyhermüller, Prof. K. Wieghardt
Max-Planck-Institut für Bioanorganische Chemie
Stiftstraße 34-36,D-45470 Mülheim an der Ruhr (Germany)
Fax: (+49) 208-306-3952
E-mail: wieghardt@mpi-muelheim.mpg.de

[b] Prof. S. D. George
Department of Chemistry and Chemical Biology
Baker Laboratory, Cornell University, Ithaca, NY 14853 (USA)

[**] mnt = maleonitriledithiolate; Et_2dtc = diethyldithiocarbamato.

Supporting information for this article is available on the WWW under http://dx.doi.org/10.1002/chem.200903381.

Complexes

$[PPh_4]_3[Fe^{III}(mnt)_3]\cdot CH_2Cl_2$	($S = {}^1/_2$)	$[PPh_4]_3$**1**$\cdot CH_2Cl_2$
$[PPh_4]_2[Fe^{IV}(mnt)_3]$	($S = 1$)	$[PPh_4]_2$**1**^{ox}
$[PPh_4]_2[Fe^{III}(Et_2dtc)(mnt)_2]$	($S = {}^1/_2$)	$[PPh_4]_2$**2**
$[PPh_4][Fe^{IV}(Et_2dtc)(mnt)_2]$	($S = 1$)	$[PPh_4]$**2**^{ox}
$[NEt_4][Fe^{III}(Et_2dtc)_2(mnt)]$	($S = {}^1/_2$)	$[NEt_4]$**3**
$[Fe^{IV}(Et_2dtc)_2(mnt)]$	($S = 1$)	**3**^{ox}
$[Fe^{III}(Et_2dtc)_3]$	($S = {}^1/_2$)	**4**
$[Fe^{IV}(Et_2dtc)_3][I_5]$	($S = 1$)	**4**$^{ox}[I_5]$

Ligands

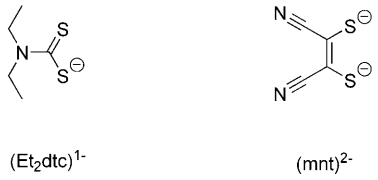

$(Et_2dtc)^{1-}$ $(mnt)^{2-}$

Scheme 1. Complexes and ligands.

oxidized species $[Fe(Et_2dtc)_{3-n}(mnt)_n]^{(n-1)-}$ (**1**^{ox}–**4**^{ox}). By using single crystal X-ray crystallography, EPR and Mössbauer spectroscopy as well as magnetochemistry and Fe and S K-edge XAS, we attempted to determine ligand and metal-ion oxidation levels experimentally. In addition, XAS and Mössbauer spectra and molecular geometries and electronic structures have been calculated by using density functional theory (BP86 and B3LYP functionals).

The following mixed-ligand complexes have been isolated previously and their electronic structures have been—in part—described: **1** and **1**^{ox} in references [14,17–20], **2** and **3** in references [22,23], **3**^{ox} in reference [23], **4** in reference [7], and **4**^{ox} in references [2,12a]. Complex **2**^{ox} has been prepared in this work for the first time. The structures of the complexes **1**^{ox}[18,19] and **4**^{ox}[9] have been determined at room temperature; that of **4** at 79 and 297 K to detect possible structural changes for its temperature-dependent spin crossover behavior ($S = {}^1/_2 \leftrightarrow {}^5/_2$). The structures of all complexes with the exception of **4**^{ox} have been (re)determined by X-ray crystallography at 100 K on the same diffractometer.

Results

Syntheses: Complexes $[PPh_4]_3[Fe^{III}(mnt)_3]\cdot CH_2Cl_2$ ($[PPh_4]_3$**1**$\cdot CH_2Cl_2$) and its one-electron oxidized analogue $[PPh_4]_2[Fe^{IV}(mnt)_3]$ ($[PPh_4]_2$**1**^{ox}) have been prepared by following the procedures reported by McCleverty[14] and Gray et al.,[17] respectively. Equimolar amounts of $[PPh_4]Br$ were used instead of the originally used $[AsPh_4]Cl$. Single crystals suitable for X-ray crystallography of both species were obtained from CH_2Cl_2/ethanol solutions.

$[PPh_4]_2[Fe^{III}(Et_2dtc)(mnt)_2]$ ($[PPh_4]_2$**2**) has also been synthesized by following the procedure developed by McCleverty et al.[22] Dark-brown crystals of $[PPh_4]_2$**2** suitable for X-ray crystallography were isolated from a concentrated MeOH/H_2O (1:1 vol) solution of $[PPh_4]_2$**2** by slow evaporation of the solvent. One-electron oxidation of the dianion **2** with one equivalent of ferrocenium hexafluorophosphate in CH_2Cl_2 afforded the monoanion $[Fe^{IV}(Et_2dtc)(mnt)_2]^{1-}$ (**2**^{ox}), which was isolated as the $[PPh_4]^+$ salt, $[PPh_4]$**2**^{ox}. Recrystallization from MeCN/H_2O (1:1 vol) yielded crystals suitable for X-ray crystallography.

The complex $[NEt_4][Fe^{III}(Et_2dtc)_2(mnt)]$ ($[NEt_4]$**3**) was generated from $[Fe^{II}(Et_2dtc)_2]$ as described by Pignolet, Holm et al.[23] Upon addition of *n*-hexane to a CH_2Cl_2 solution of $[NEt_4]$**3** and slow evaporation of the solvents, single crystals suitable for X-ray crystallography were obtained. The corresponding neutral complex $[Fe^{IV}(Et_2dtc)_2(mnt)]$ (**3**^{ox}) was prepared by oxidation of the anion **3** with ferrocenium hexafluorophosphate.

Finally, the neutral $[Fe^{III}(Et_2dtc)_3]$ (**4**) was synthesized as described in reference [7].

Crystal structures: Of the eight complexes **1**–**4** and **1**^{ox}–**4**^{ox} only the crystal structures of **1**^{ox},[18,19] **4**,[10] and **4**^{ox}[9] have been determined previously at room temperature. The structure of **4** has also been determined at 79 K.

To obtain a better resolution with significantly smaller standard deviations, we have (re)determined the structures of $[PPh_4]_3$**1**$\cdot CH_2Cl_2$, $[PPh_4]_2$**1**^{ox}, $[PPh_4]_2$**2**, $[PPh_4]$**2**^{ox}, $[NEt_4]$**3**, **3**^{ox}, and **4** at 100(2) K. The crystallographic details are summarized in the Experimental Section and Tables S1–S4 (Supporting Information) give selected bond lengths and angles.

The trianion in crystals of $[PPh_4]$**1**$\cdot CH_2Cl_2$ consists of three bidentate $(mnt)^{2-}$ ligands and a central iron ion (Figure 1). In tris(chelate) complexes, two triangular faces perpendicular to the approximate C_3 axis can be defined as shown in Figure 2. For **1**, these two triangular faces are defined by vertices comprising S(1), S(11), S(21) and S(4), S(14), S(24), respectively, one from each chelate ligand. The twist angle Θ (Figure 2) was determined individually for each chelate ligand by measuring the chelate projection angle along the approximate C_3 axis. For a perfect octahedron, Θ between two bridged corners of the two triangles is 60°; a rotation about the C_3 axis leads to a trigonal distortion. In the limiting case of $\Theta = 0°$, the three chelate ligands form a regular trigonal prism. The average magnitude of Θ_{av} in **1** is 53.4° resulting in a weakly distorted octahedral geometry of the FeS_6 polyhedron.

The Fe–S bond lengths are in the range of 2.2500(6)–2.3242(6) Å. Three long bonds ($Fe-S_{av} = 2.323$ Å) are found for the S(1), S(4), S(14) face, whereas the opposing face shows significantly shorter bonds ($Fe-S_{av} = 2.260$ Å), resulting in a trigonal elongation of the octahedron. Note that this distortion is not along the approximate C_3 axis of the molecule. It will be shown below that it corresponds to a Jahn–

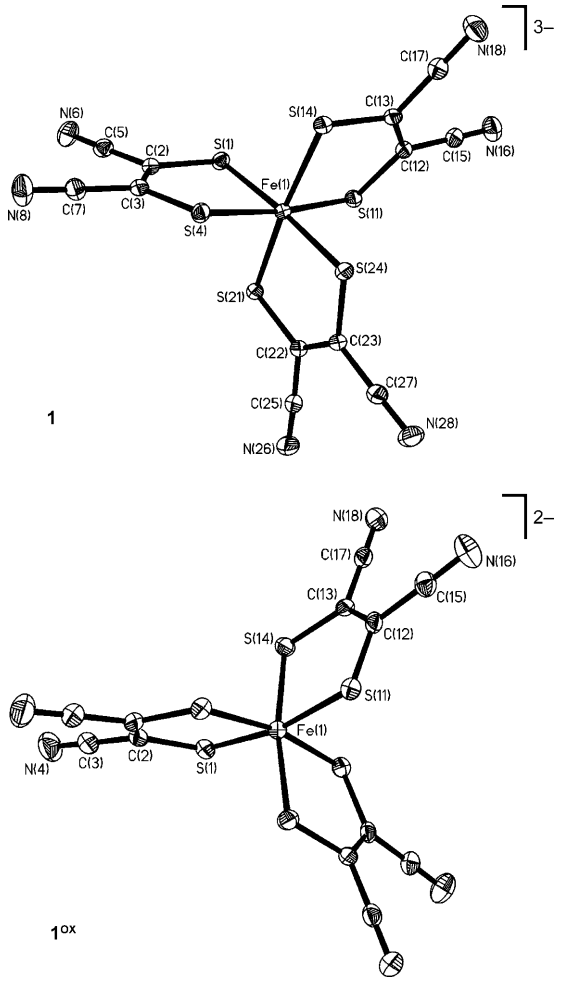

Figure 1. Structure and labeling scheme of the trianion **1** in $(PPh_4)_3$**1**·CH_2Cl_2 and the dianion $\mathbf{1}^{ox}$ in $(PPh_4)_2\mathbf{1}^{ox}$. Thermal ellipsoids are drawn at the 50% probability level.

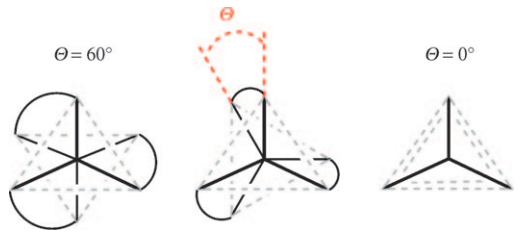

Figure 2. Representation of the twist angle Θ and the two limiting cases of octahedral (left) and trigonal prismatic (right) geometry.

Teller distortion of the system. The average C–S bond length at 1.735 Å and the average C–C bond length at 1.368 Å, which indicates the presence of closed-shell dianionic mnt^{2-} ligands,[19,24] requiring a ferric central metal ion.

The structure of the one-electron oxidized dianionic species $\mathbf{1}^{ox}$ possesses a molecular structure that is very similar to that of **1**. However, the average trigonal twist of the $(mnt)^{2-}$ ligands is smaller ($\Theta_{av} = 46.6°$) than that in **1** and the trigonal Jahn–Teller distortion is absent. Therefore, $\mathbf{1}^{ox}$ contains a crystallographic C_2 axis perpendicular to the approximate C_3 axis of the molecule. The Fe–S bond lengths are in the narrow range of 2.2682(7)–2.2822(7) Å with an average distance of 2.274 Å, which is slightly shorter than those in **1**. Surprisingly, the ligand bond distances remain virtually unchanged upon oxidation from **1** to $\mathbf{1}^{ox}$ with an average C–S bond length of 1.733 Å and an average C–C bond distance at 1.363 Å. This suggests that the oxidation is metal rather than ligand-centered. Thus the structural parameters of **1** and $\mathbf{1}^{ox}$ indicate the presence of a low-spin ferric ion ($S_{Fe} = {}^1/_2$; d^5) in **1** and an Fe^{IV} ion in $\mathbf{1}^{ox}$ ($S_{Fe} = 1$; d^4).

The complexes **2** and $\mathbf{2}^{ox}$ both contain two mnt and one Et_2dtc ligand (Figure 3). The average Fe–S bond length in **2** is 2.255 Å for mnt, in which the bonds in the *trans* position to the second mnt ligand are slightly longer resulting in a pseudo-axial distortion. The average C–S and C–C bonds (1.744 and 1.373 Å) of the mnt ligands are indicative of the closed-shell dianionic form $(mnt)^{2-}$. The Et_2dtc ligand shows significantly longer Fe–S bond lengths (2.360 Å). The intraligand distances are in agreement with the values reported for the uncoordinated monoanionic closed-shell form of the ligand.[25] Considering the total charge this implies that **2** contains an Fe^{III} center. The twist angle Θ is significantly different for the two types of bidentate chelate ligands in **2**. It has been shown that for a given chelate ligand the upper limit of Θ depends on the normalized bite, *b*, which is defined as the distance between the donor atoms of the chelate divided by the metal–donor atom distance.[26] Ligands

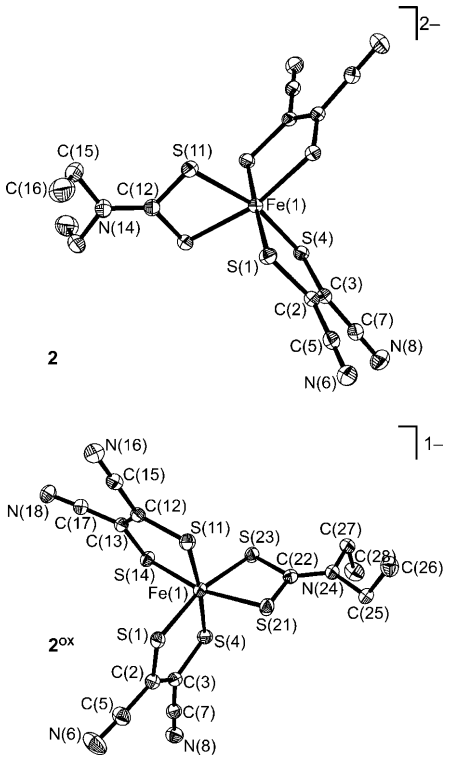

Figure 3. Structure and labeling scheme of the dianion **2** in $(PPh_4)_2$**2** and the monoanion $\mathbf{2}^{ox}$ in $(PPh_4)\mathbf{2}^{ox}$. Thermal ellipsoids are drawn at the 50% probability level. Hydrogen atoms are omitted for clarity.

with small normalized bites cannot reach perfect octahedral geometry ($\Theta = 60°$). Since Et_2dtc forms only four-membered rings and shows long Fe–S distances, its bite is small relative to mnt. This can also be observed in the S-Fe-S angles for the three ligands (see Table S2 in the Supporting Information). Consequently, the magnitude of Θ in **2** is significantly smaller for Et_2dtc (43.9°) than for mnt (50.3°).

Upon oxidation to $\mathbf{2^{ox}}$, the average Fe–S bond length decreases for both ligands (mnt: 2.255, Et_2dtc: 2.330 Å), whereas the structural parameters of the ligands remain almost unaltered. This indicates again that the oxidation is metal-centered and that $\mathbf{2^{ox}}$ contains an Fe^{IV} ion. In contrast to **2**, the Fe–S distances of mnt in the *trans* position to the second mnt ligand are now slightly shorter than the bonds in the *cis* position. The twist angle Θ for the two different ligand types decreases slightly upon oxidation, but the effect is less pronounced than for **1** versus $\mathbf{1^{ox}}$.

In **3** and $\mathbf{3^{ox}}$ a second mnt ligand has been exchanged for Et_2dtc (Figure 4). Note that for $\mathbf{3^{ox}}$, one of the Et_2dtc ligands

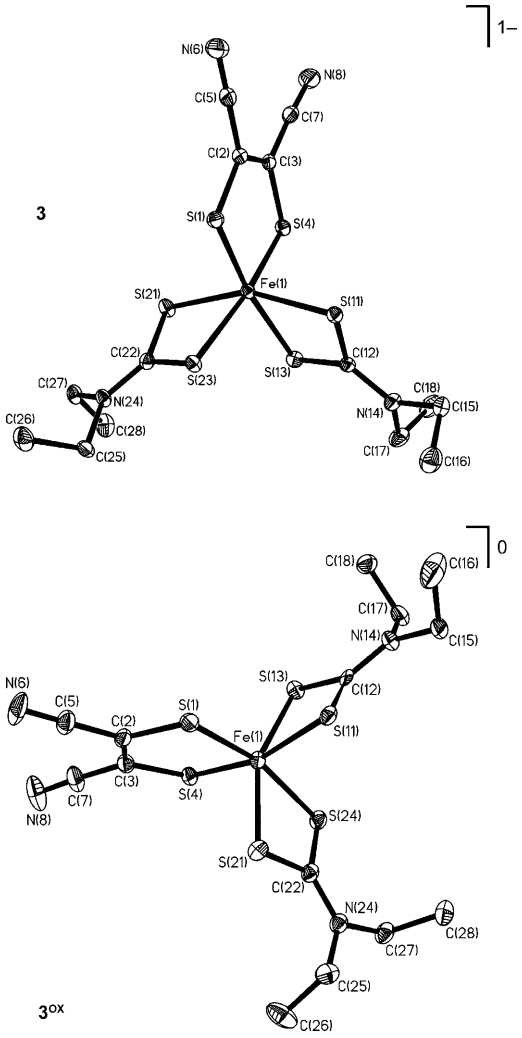

Figure 4. Structure and labeling scheme of the monoanion **3** in (NEt_4)**3** and neutral $\mathbf{3^{ox}}$. Thermal ellipsoids are drawn at the 50% probability level. Hydrogen atoms are omitted for clarity.

(containing S(11) and S(13)) is strongly disordered leading to large errors in the estimated standard deviations. For both complexes, the intraligand bond distances indicate closed-shell dianionic mnt and monoanionic Et_2dtc ligands. Therefore, the oxidation is again metal-centered and the compounds **3** and $\mathbf{3^{ox}}$ contain Fe^{III} and Fe^{IV} centers, respectively. Similar to the oxidation from **1** to $\mathbf{1^{ox}}$, the twist angle Θ decreases significantly upon oxidation for both ligands. The average Fe–S bond lengths in **3** are 2.210 (mnt) and 2.321 Å (Et_2dtc), which are nearly the same as 2.227 and 2.313 Å in the oxidized form $\mathbf{3^{ox}}$.

The molecular structures of **4** and $\mathbf{4^{ox}}$ have been reported previously.[9,10,14] For **4**, a structure of higher quality was obtained in this work (Figure 5). Unfortunately, complex $\mathbf{4^{ox}}$

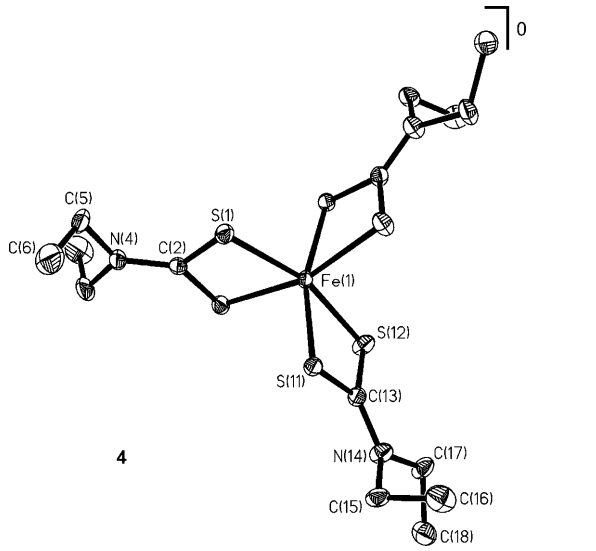

Figure 5. Structure and labeling scheme of **4**. Thermal ellipsoids are drawn at the 50% probability level. Hydrogen atoms are omitted for clarity.

could not be isolated as suitable single crystals, precluding a re-examination of its structural parameters. The structural parameters of **4** and $\mathbf{4^{ox}}$ are summarized in Table S4 (Supporting Information). The bond lengths in both compounds are identical within 3σ and the structural parameters of the ligand are indicative of closed-shell monoanionic $(Et_2dtc)^{1-}$, reflecting metal-centered oxidation from **4** to $\mathbf{4^{ox}}$. Compound **4** shows a strong trigonal distortion of the octahedron with an average twist Θ_{av} of 40.53°. The geometry of the cation $\mathbf{4^{ox}}$ is intermediate between octahedral and trigonal prismatic ($\Theta_{av} = 32.95°$).

In summary, the eight-membered series of heteroleptic Et_2dtc/mnt iron complexes has been fully structurally characterized. A comparison of important structural parameters is given in Table 1. Some general structural trends within the series are identified:

1) The average Fe–S bond length for both types of ligand increases with the number of mnt ligands in the molecule.

Table 1. Comparison of selected average bond distances [Å] and angles [°] for the Fe^{III} complexes **1–4** and the Fe^{IV} complexes $\mathbf{1^{ox}}$–$\mathbf{3^{ox}}$.

		Fe–S_{av}	S–C_{av}	C–C_{av}	C–N_{av}	Θ	Θ_{av}
1		2.287	1.753	1.368		53.40	53.40
$\mathbf{1^{ox}}$		2.274	1.733	1.363		46.64	46.64
2	Et_2dtc	2.360	1.719		1.326	43.87	48.18
	mnt	2.268	1.744	1.373		50.33	
$\mathbf{2^{ox}}$	Et_2dtc	2.330	1.727		1.316	40.51	46.37
	mnt	2.255	1.733	1.374		49.30	
3	Et_2dtc	2.321	1.709		1.324	42.77	44.63
	mnt	2.209	1.729	1.373		48.35	
$\mathbf{3^{ox}}$	Et_2dtc	2.313	1.730		1.317	38.30	39.14
	mnt	2.227	1.733	1.373		40.83	
4		2.305	1.719		1.331	40.53	40.53
$\mathbf{4^{ox}}$		2.299	1.714		1.292	32.95	32.95

2) Θ_{av} decreases with the number of *S*,*S*′-coordinated $(Et_2dtc)^{1-}$ ligands, giving more trigonally distorted octahedra.
3) The individual twist angles Θ for both ligands decrease upon oxidation.
4) The structural parameters of the ligands show very little variation throughout the series, which indicates that all redox processes are entirely metal-centered and that the oxidized complexes $\mathbf{1^{ox}}$–$\mathbf{4^{ox}}$ are genuine FeIV species.

Electrochemistry: The electrochemical parameters of **1**, **3**, and **4** have been reported before by McCleverty[14,22] and Martin et al.[11] However, differing experimental conditions (solvents, electrodes, electrolytes) complicate a concise comparison of the redox properties within the series. Therefore, we have reinvestigated the redox properties for the whole series by cyclic voltammetry in CH_2Cl_2 with a glassy carbon working electrode and $[N(n\text{Bu})_4]PF_6$ as the supporting electrolyte (0.1 M). All potentials are referenced against the ferrocenium/ferrocene (Fc^+/Fc) couple by using ferrocene as an internal standard. The resulting CVs are shown in Figure S1 (Supporting Information) and the potentials are given in Table 2. All complexes **1–4** show a reversible redox feature corresponding to a one-electron oxidation to $\mathbf{1^{ox}}$–$\mathbf{4^{ox}}$, which was shown by controlled-potential coulometry. The position of this redox feature correlates nicely with the number of $(mnt)^{2-}$ ligands in the complex. While it is observed at −171 mV for the homoleptic Et_2dtc^- complex **4**, it shifts to more a negative potential by ~200 mV per mnt^{2-} ligand, corresponding to easier oxidation. The potentials for **3**, **2**, and **1** are −335, −569, and 753 mV, respectively (Figure 6). This trend reflects the increased π donor strength of $(mnt)^{2-}$ relative to $(Et_2dtc)^-$, which destabilizes the t_{2g} set of the low-spin complexes and, therefore, facilitates oxidation.

Table 2. Electrochemical properties of **1–4** [V] versus Fc^+/Fc.

	$E^{red}_{1/2}$	$E^{ox1}_{1/2}$	$E^{ox2}_{1/2}$
1	–[a]	−0.75	0.25[b]
2	–[a]	−0.57	0.34
3	–[a]	−0.34	0.70[b]
4	−1.05	−0.17	–[a]

[a] Not observed in the measured potential range. [b] Oxidation peak potential.

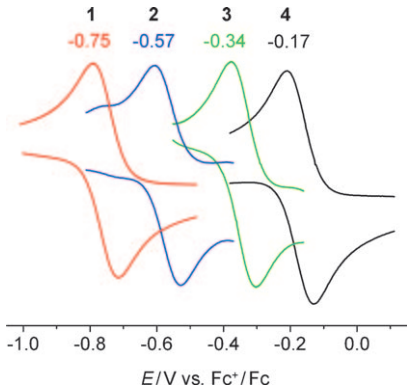

Figure 6. Comparison of the redox potentials for the one-electron oxidations of **1–4** to $\mathbf{1^{ox}}$–$\mathbf{4^{ox}}$.

Accordingly, **4** shows a reversible redox wave for the reduction from Fe^{III} to Fe^{II} at −1046 mV, whereas **1–3** show only irreversible processes. Instead, **1–3** exhibit an additional feature corresponding to a second oxidation at high potentials, which is quasi-reversible on the CV timescale (200 mVs^{-1}).

Magnetochemistry: The electronic ground states of the ferric complexes **1–4** have been established from variable-temperature (400–300 K) magnetic susceptibility measurements on powders by using a SQUID magnetometer with an applied field of 1.0 T. The temperature dependence of the effective magnetic moment, μ_{eff}, of the four compounds is shown in Figure S2 (Supporting Information). At low temperatures, in the range of 10–150 K, **1–4** show nearly temperature-independent magnetic moments in the narrow range of 1.8–2.0 μ_B indicative of a common $S = {}^1/_2$ ground state. Interestingly, the g_{av} value (Table 3) is in the narrow range of 2.05 for **1**, 2.10 for **2**, and 2.14 for **3**, but it is 2.35 for **4**. These values are in excellent agreement with those measured by EPR spectroscopy in frozen solution (see below). Below 10 K, μ_{eff} decreases slightly due to field saturation

Table 3. Spin-Hamiltonian parameters for simulations of the magnetic susceptibility measurements of **1–4** and $\mathbf{1^{ox}}$–$\mathbf{3^{ox}}$.

	S	g_{av}	D [cm^{-1}]	θ [K]	χ_{TIP} [10^{-6} emu]	PI [%][a]
1	${}^1/_2$	2.050	–	−0.2	300	0.6
2	${}^1/_2$	2.100	–	−0.6	300	1.0
3	${}^1/_2$	2.139	–	−0.4	110	0.0
4	${}^1/_2$	2.350	–	−1.0	800	2.2
$\mathbf{1^{ox}}$	1	2.020	10	0.0	185	–
$\mathbf{2^{ox}}$	1	2.001	−25	−0.3	610	–
$\mathbf{3^{ox}}$	1	2.000	−68	0.0	600	–

[a] Paramagnetic impurity with $S = {}^5/_2$ ground state and identical molecular weight.

and weak intermolecular antiferromagnetic coupling. This effect is strongest in the neutral complex **4**, in which the molecules are not separated by countercations and, therefore, exhibit more direct intermolecular interactions. The low-temperature region (2–150 K) was readily simulated for **1**–**4** by using a mean field approximation with a Weiss temperature θ as listed in Table 3. At higher temperatures, μ_{eff} increases for **1**–**4**. This phenomenon has first been observed for tris(dithiocarbamates) like **4** by Cambi and Cagnasso,[27] and was intensively studied by a wide range of physical methods.[10,12,13,28,29] It can be unambiguously attributed to a thermal spin crossover from low-spin Fe^{III} ($S=^1/_2$) to high-spin Fe^{III} ($S=^5/_2$) in the solid state. This spin crossover is observed at temperatures above 150 K for **4**. For **1**, **2**, and **3** it can only be observed above 200, 180, and 240 K, respectively (see Figure S2 in the Supporting Information).

The plots of μ_{eff} versus T for $\mathbf{1}^{ox}$, $\mathbf{2}^{ox}$, and $\mathbf{3}^{ox}$ are shown in Figure 7. The insets show the isofield magnetization measurements at variable temperatures. The magnetic moments of $\mathbf{1}^{ox}$, $\mathbf{2}^{ox}$, and $\mathbf{3}^{ox}$ are constant in the range from 50–290 K at 2.86, 2.80, and 2.81 μ_B, respectively, which indicates a spin-triplet ground state ($S=1$). Below 50 K, μ_{eff} decreases due to magnetization saturation at 1 T and the influence of zero-field splitting. The sign of D for $\mathbf{1}^{ox}$, $\mathbf{2}^{ox}$, and $\mathbf{3}^{ox}$ was determined from the isofield magnetization measurements. The fitting parameters are summarized in Table 3. The spin ground state of $\mathbf{4}^{ox}$ has been reported to be $S=1$.[2] It is important to note that no evidence for a singlet–triplet spin-state equilibrium has been observed in this Fe^{IV} series as has been suggested previously from incomplete magnetic susceptibility measurements of $\mathbf{3}^{ox}$ in the temperature range 80–400 K. The observed drop of μ_{eff} with decreasing temperature (< 120 K) is due to large zero-field splitting $D=-68\ cm^{-1}$ as has been unequivocally established here by the field dependent magnetization data. Similar results have been reported for $\mathbf{1}^{ox}$.[13]

EPR spectroscopy: The X-band EPR spectra of **1**–**4** are shown in Figure S3 (Supporting Information). The spectrum of **1** has been reported earlier;[15] the values found in this work are in agreement with the published data. The data clearly confirm that under the experimental low-temperature conditions (T < 50 K) all compounds are in their $S=^1/_2$ ground state. The complexes exhibit rhombic spectra with three clearly distinguishable g values around $g=2$. The spectra of **1**–**3** show significant g anisotropy in agreement with a low-spin Fe^{III} (d^5) description. They were readily simulated by using the principal g values given in Table 4. The spectrum of **4** shows even larger g anisotropy. This has first been observed and discussed by Hall and Hendrickson.[28] The spectrum is very similar to the spectrum of $[Fe^{III}(cyclam)(Et_2dtc)]^{2+}$ reported in reference [21] and can be classified as a highly anisotropic low-spin (HALS) spectrum.[30,31] These spectra are typically found and well-studied for octahedral hemes with axial symmetry,[30] but examples of non-heme compounds are rare and have only been reported recently.[21,32] The large anisotropy is indicative of a pair of almost degenerate d orbitals yielding large orbital contributions to the magnetic moment of the electron. Due to the unusual lineshape often observed for HALS spectra it has not been possible to obtain satisfactory fits of the spectrum by using Gaussian or Lorentzian lineshapes with the usual angular-dependent line widths. Therefore, the three g values

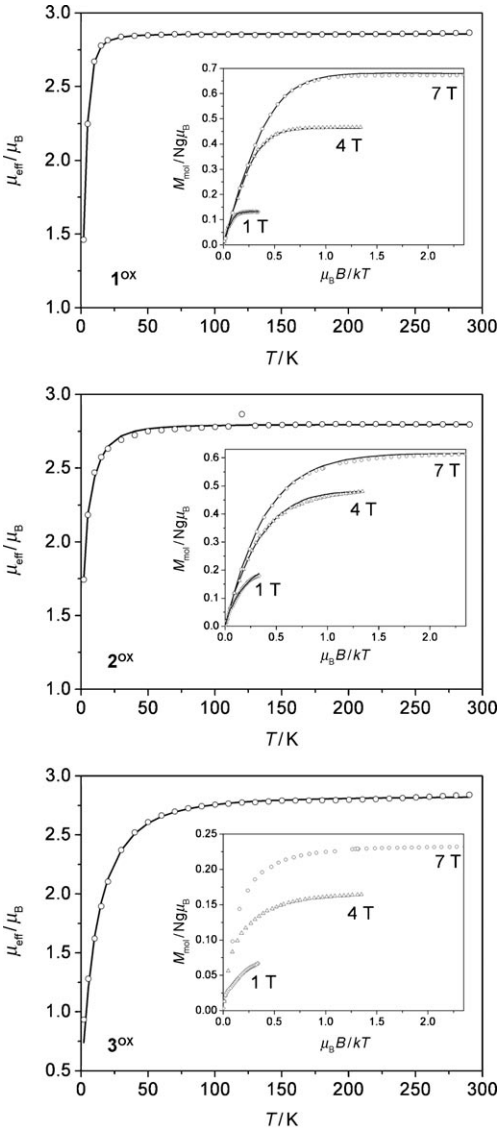

Figure 7. Temperature dependence of the magnetic moment, μ_{eff}, of $\mathbf{1}^{ox}$ (top), $\mathbf{2}^{ox}$ (middle), and $\mathbf{3}^{ox}$ (bottom). —— is a simulation for $S=1$ with parameters as given in Table 3. The insets show the magnetization data at 1, 4, and 7 T.

Table 4. Comparison of the anisotropic g values of **1**–**4** from EPR measurements.

	g_{max}	g_{mid}	g_{min}	g_{av}[a]
1	2.27	2.09	1.97	2.114
2	2.19	2.11	2.00	2.101
3	2.22	2.12	2.00	2.112
4	3.38	1.79	1.15	2.306

[a] $g_{av}=\{1/3(g_{max}^2+g_{mid}^2+g_{min}^2)\}^{1/2}$.

were read off the experimental trace as approximate values of 3.38, 1.79, and 1.15. The high g_{av} value of 2.31 is in excellent agreement with the magnetic susceptibility data.

Mössbauer spectroscopy: Figure S4 (Supporting Information) shows the zero-field Mössbauer spectra of **1**–**4** and the one-electron oxidized complexes $\mathbf{1}^{ox}$–$\mathbf{4}^{ox}$ at 80 K. The line broadening in the spectra of **1** and **2** is a result of intermediate spin relaxation and decreases at elevated temperatures. The isomer shifts, δ, and the absolute value of the quadrupole splittings, $|\Delta E_Q|$, are summarized in Table 5. For the

Table 5. Summary of the Mössbauer parameters for **1**–**4** and $\mathbf{1}^{ox}$–$\mathbf{4}^{ox}$ at 80 K.

	δ [mm s^{-1}][a]	$\lvert\Delta E_Q\rvert$ [mm s^{-1}][b]		δ [mm s^{-1}][a]	$\lvert\Delta E_Q\rvert$ [mm s^{-1}][b]
1	0.36	1.68	$\mathbf{1}^{ox}$	0.24	1.56
2	0.39	1.77	$\mathbf{2}^{ox}$	0.25	1.70
3	0.41	1.82	$\mathbf{3}^{ox}$	0.28	1.98
4	0.47	0.70[c]	$\mathbf{4}^{ox}$	0.30	2.48[c]

[a] Isomer shift vs. α-Fe at 298 K. [b] Quadrupole splitting. [c] See also references [12] and [13].

low-spin Fe^{III} complexes **1**–**4**, δ increases throughout the series with the number of $(Et_2dtc)^{1-}$ ligands from 0.36 in **1** to 0.47 mm s^{-1} in **4**. Similarly, $|\Delta E_Q|$ increases with the number of $(Et_2dtc)^{1-}$ ligands from **1** (1.68 mm s^{-1}) to **3** (1.82 mm s^{-1}), but drops significantly for **4** (0.70 mm s^{-1}). The small quadrupole splitting in **4** is the result of the presence of two almost degenerate t_{2g} orbitals resulting from a trigonally twisted FeS_6 polyhedron, and is in agreement with the electronic structure deduced from EPR spectroscopy.

Upon oxidation, δ increases for all compounds ($\Delta\delta_N = \delta_N - \delta_N^{ox}$ with N = **1**–**4**). The effect is most pronounced in **4** versus $\mathbf{4}^{ox}$ ($\Delta\delta_4 = 0.17$ mm s^{-1}) and smallest for **1** versus $\mathbf{1}^{ox}$ ($\Delta\delta_1 = 0.12$ mm s^{-1}) with average values for **2** versus $\mathbf{2}^{ox}$ ($\Delta\delta_2 = 0.14$ mm s^{-1}) and **3** versus $\mathbf{3}^{ox}$ ($\Delta\delta_3 = 0.13$ mm s^{-1}). Since Mössbauer spectroscopy is a local probe for the electronic structure at the iron nucleus, this shift indicates a metal-centered oxidation for **1**–**4**, resulting in the formation of the genuine $S = 1$ Fe^{IV} species $\mathbf{1}^{ox}$–$\mathbf{4}^{ox}$. However, the decreasing values for $\Delta\delta_N$ from **4** to **1** indicate that the strong π-donor $(mnt)^{2-}$ is not completely innocent, but transfers some electron density to the metal center. Nevertheless, the shift is too large to support an $[Fe^{III}(mnt^{2-})_2(mnt^{\bullet-})]^{2-}$ description for $\mathbf{1}^{ox}$.

The quadrupole splittings remain almost constant upon oxidation with the exception of **4** versus $\mathbf{4}^{ox}$, in which the relatively large change is due to the particular electronic structure of **4**. The magnitude of $|\Delta E_Q|$ decreases in the order $\mathbf{4}^{ox} > \mathbf{3}^{ox} > \mathbf{2}^{ox} > \mathbf{1}^{ox}$, which is again attributed to increasing covalency. Whereas $\mathbf{4}^{ox}$ shows a quadrupole splitting of 2.48 mm s^{-1}, which is close to the expectation value for two holes in the t_{2g} shell (~2.40 mm s^{-1}), $|\Delta E_Q|$ decreases with an increasing number of $(mnt)^{2-}$ ligands to 1.56 mm s^{-1} in $\mathbf{1}^{ox}$.

X-ray absorption spectroscopy: The Fe K-edge X-ray absorption spectra of **1** and $\mathbf{1}^{ox}$ are shown in Figure 8. The corresponding spectra of **2**–**4** and $\mathbf{2}^{ox}$–$\mathbf{3}^{ox}$ are shown in Figure S5

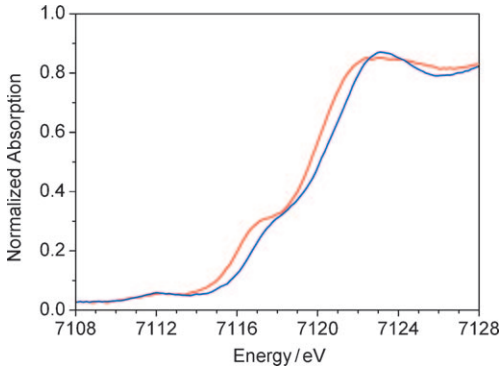

Figure 8. Normalized Fe K-edge X-ray absorption spectra of **1** and $\mathbf{1}^{ox}$. ——: **1**, ——: $\mathbf{1}^{ox}$.

(Supporting Information). The rising edge positions determined at the first inflection point of the edge and the pre-edge energies are summarized in Table 6. A one-electron oxidation of **1**–**3** results in a shift of the rising edge energy of 0.8, 0.7, and 0.9 eV, respectively. The rising edge is a good measure of the effective nuclear charge at the metal ion and supports a metal-centered oxidation (~1 eV per oxidation state) to an Fe^{IV} ion.

Table 6. Fe K-edge XAS rising edge and pre-edge energies for **1**–**4** and $\mathbf{1}^{ox}$–$\mathbf{3}^{ox}$.

	Rising edge energy [eV][a]	Pre-edge energy [eV]
1	7116.1	7112.0
$\mathbf{1}^{ox}$	7116.9	7112.3
2	7115.6	7112.0
$\mathbf{2}^{ox}$	7116.3	7112.2
3	7115.4	7112.1
$\mathbf{3}^{ox}$	7116.3	7112.3
4	7115.5	7112.1

[a] Determined at the first inflection point.

In this series of compounds, the pre-edge region does not reflect a change in the oxidation state of the Fe ion; the pre-edge peak energy is constant at 7112.1 ± 0.2 eV. In contrast to complexes $[Fe^{III}(cyclam)(Et_2dtc)]^{2+}$, $[Fe^{III}(cyclam)(tdt)]^{+}$ (tdt = toluene-3,4-dithiolene), and $[Fe^{III}(cyclam)(tdt^{\bullet})]^{2+}$ ($S = 0$),[21] the geometry of the first coordination shell of **1**–**4** changes significantly upon oxidation. Since the pre-edge features result from transitions to the Fe 3d orbitals they are sensitive to changes in the ligand field and hence the geometry. For XAS the empty e_g (or e″) orbitals are of interest. As a result of the larger trigonal twist, the energy of the empty e″ orbitals is lowered upon oxidation, whereas the energy of the Fe 1s orbital is not affected due to its spherical symmetry. Consequently, the trigonal twist lowers the pre-edge

transition energy, which counteracts the expected ~1 eV increase in pre-edge energy upon oxidation of the metal (Table 6).

The S K-edge XAS spectra of **1**–**4** and **1^{ox}**–**3^{ox}** are shown in Figure S6 (Supporting Information). All compounds show multiple, overlapping pre-edge and near-edge features in the region from 2469–2473 eV. Therefore, deconvolution of the spectra by pseudo-Voigt fitting is necessary. The interpretation is further complicated by the fact that four of the complexes are heteroleptic and contain two different sulfur donor ligands, which increases the number of possible transitions.

To obtain a better understanding of the possible transitions, the XAS spectra of the sodium salts of the free ligands were investigated first (Table 7). Sarangi et al.[33] have reported the S K-edge spectrum of $Na_2(mnt)$. In contrast to other dianionic dithiolene ligands, $(mnt)^{2-}$ shows a pre-edge peak at 2471.1 eV assigned as a transition to a π* orbital that is significantly stabilized relative to other dithiolenes by the strongly electron-withdrawing cyano groups. The dipole-allowed edge-feature is observed at 2472.3 eV in $(mnt)^{2-}$. The deconvoluted S K-edge spectrum of $NaEt_2dtc{\cdot}3H_2O$ is shown in Figure 9. Surprisingly, $(Et_2dtc)^{1-}$ also shows a pre-edge transition at 2471.4 eV, which can be identified as a transition to the empty π* orbital of the free ligand. The edge-feature for $(Et_2dtc)^{-}$ is found at 2473.0 eV. The effect of metal coordination is reflected in the S K-edge spectra of $[Fe^{III}(cyclam)(Et_2dtc)]^{2+}$ and $[Fe^{III}(cyclam)(mnt)]^{+}$, wherein a single $(Et_2dtc)^{-}$ or $(mnt)^{2-}$ ligand is coordinated to a low-spin Fe^{III} center, respectively. The spectra (Figure 9) show two additional peaks, resulting in a total of three pre-edge peaks. For $[Fe^{III}(cyclam)(Et_2dtc)]^{2+}$, the lowest energy feature at 2470.1 eV can be assigned to a transition to the half-filled t_{2g} orbital of the d^5 low-spin system. The very low intensity indicates only small sulfur contributions to this orbital, reflecting the poor π-donor strength of the dithiocarbamate ligand. The second peak at 2471.1 eV stems from transitions to the empty e_g orbitals (Fe–S σ*), which gain intensity through covalency (S 3p contributions). The third transition at 2472.3 eV is due to the empty π* orbital of the ligand that was observed for the free ligand; however, shifted 0.9 eV to higher energy in $[Fe^{III}(cyclam)(Et_2dtc)]^{2+}$. The edge feature is also shifted to higher energy and is found at 2473.6 eV. These shifts are the result of coordination to the Lewis acidic metal center, which removes electron density from the ligand and creates more electron deficient (oxidized) sulfur donor atoms. The spectrum of $[Fe^{III}(cyclam)(mnt)]^{+}$ can be interpreted in a similar way. However, the transition to the t_{2g} SOMO at 2470.2 eV shows a higher intensity, due to stronger π interactions between the metal and the ligand, which lead to an increased sulfur 3p contribution to this orbital. The peak at 2470.9 eV can again be assigned to a transition to the Fe–S antibonding e_g orbitals. Similar to the Et_2dtc complex, the transition to the mnt π* orbital at 2471.9 eV and the edge feature at 2473.3 eV are shifted by 0.8 and 1.0 eV relative to the free ligand, respectively.

With this information at hand it is possible to interpret the spectra of the homoleptic complexes **1**, **1^{ox}**, and **4** (Figure 10, Table 7). The deconvoluted S K-edge spectrum

Table 7. Energies of the pre-edge transitions and the dipole allowed edge feature.

	$E(t_{2g})$ [eV]	$E(e_g)$ [eV]	$E(L_{\pi^*})$ [eV]	E(edge feature) [eV]
1	2470.5	2470.9	2471.5	2472.9
1^{ox}	2470.3	2470.6	2471.8	2473.3
4	2470.2	2471.1	2472.0	2473.4
$Na(Et_2dtc)$	–	–	2471.4	2473.0
$Na_2(mnt)$[a]	–	–	2471.1	2472.3
$[Fe(cyclam)(Et_2dtc)]^{2+}$	2470.2	2471.1	2472.3	2473.6
$[Fe(cyclam)(mnt)]^{+}$	2470.2	2470.9	2471.9	2473.3

[a] From reference [33].

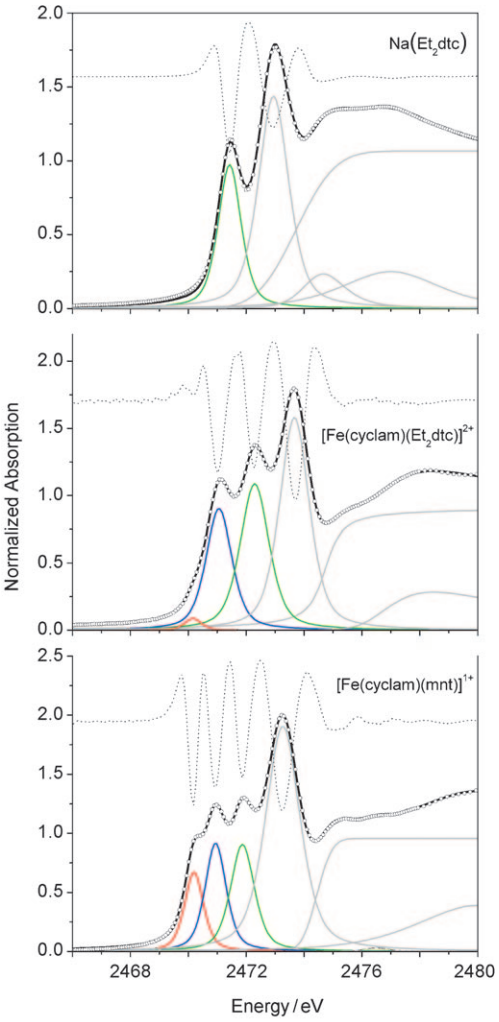

Figure 9. Pseudo-Voigt fits to the S K-edge data of $Na(Et_2dtc)$ (top), $[Fe(cyclam)(Et_2dtc)]^{2+}$ (middle), and $[Fe(cyclam)(mnt)]^{1+}$ (bottom). —— represents the transition to the empty ligand π* orbital, —— corresponds to transitions into the empty e_g orbitals, and —— represents transitions to the half-filled t_{2g} orbitals. The second derivative of the experimental data is shown by the dotted line.

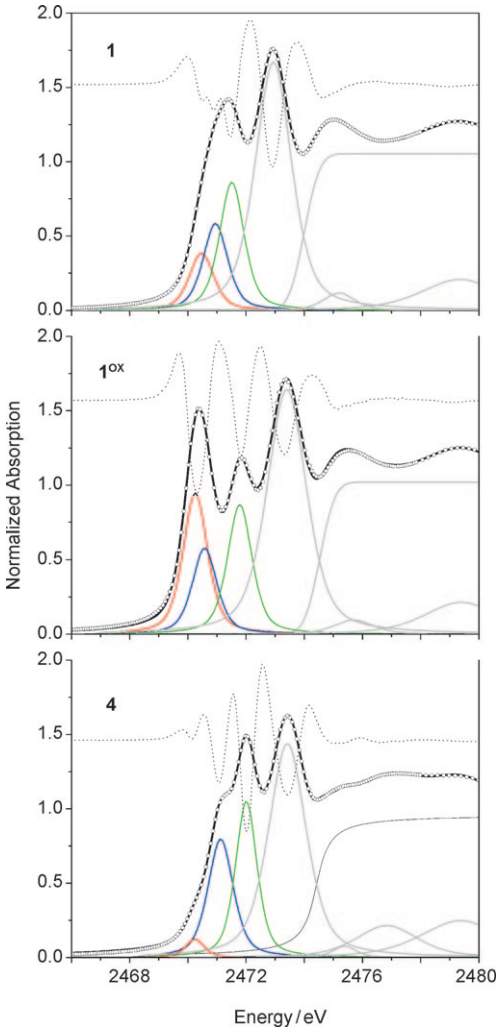

Figure 10. Pseudo-Voigt fits to the S K-edge data of **1** (top), **1**^{ox} (middle), and **4** (bottom). —— represents the transition to the empty ligand π* orbital, —— corresponds to transitions into the empty e_g orbitals, and —— represents transitions to the half-filled t_{2g} orbitals. The second derivative of the experimental data is shown by the dotted line.

of **4** displays three pre-edge peaks, which can be assigned as transitions to the half-filled t_{2g} orbital (2470.2 eV), the empty Fe–S antibonding e_g orbitals (2471.1 eV), and the π* orbitals of the ligands (2472.0 eV). Additionally, the edge-feature is observed at 2473.4 eV. The spectrum reflects an Fe^{III} low-spin configuration as in $[Fe^{III}(cyclam)(Et_2dtc)]^{2+}$ shown in Figure 9.

The deconvoluted S K-edge spectra of **1** and **1**^{ox} are shown in Figure 10. Even though only one pre-edge feature is resolved for **1**, the analysis of the second derivative of the experimental data clearly shows that it is composed of three peaks at 2470.5, 2470.9, and 2471.5 eV, which are assigned to transitions into the t_{2g}, e_g, and the ligand π* orbital, respectively. For **1**^{ox}, two pre-edge features are clearly resolved. However, the deconvolution with only two pseudo-Voigt peaks leads to an unreasonably large linewidth for the first pre-edge feature. The incorporation of a third peak improved the quality of the fit significantly and accounts nicely for the slight asymmetry of the first pre-edge peak. Relative to **1**, the transitions to the e_g set (2470.6 eV) and the ligand π* orbital (2471.8 eV) retain their intensities, whereas the intensity of the peak resulting from transitions to the t_{2g} set increases significantly. This is in good agreement with a metal-centered oxidation from a low-spin Fe^{III} to a low-spin Fe^{IV} ion creating a second hole in the t_{2g} shell. Further evidence for a metal-centered oxidation is provided by the transition energies of **1**^{ox} relative to **1**. Due to the higher effective nuclear charge of the Fe^{IV} ion in **1**^{ox}, the metal d orbitals are stabilized and the resulting transitions are shifted to lower energy. At the same time, the separation of the transitions to the metal-centered orbitals decreases, which is a result of the larger trigonal twist in **1**^{ox}, which decreases the splitting of the e_g and t_{2g} set. In contrast, the transitions to the ligand-centered π* orbital and edge feature are shifted to higher energy, which indicates a more oxidized ligand. This indicates that the ligand is not simply a spectator of the redox process. However, the shifts are too small (0.4 eV) to support a purely ligand-centered oxidation. Note that the shift in the edge feature is 0.9 eV for the ligand-centered oxidation of $[Fe^{III}(cyclam)(tdt)]^+$ to $[Fe^{III}(cyclam)(tdt^{\bullet})]^{2+}$[21]. Therefore, the S K-edge spectra support the $[Fe^{IV}(mnt)_3]^{2-}$ formulation for **1**^{ox}, but indicate significant ligand–metal covalency.

The deconvoluted S K-edge spectra of **2** and **2**^{ox} are shown in Figure S7 (Supporting Information). The edge-feature is clearly resolved for both complexes. It is observed at 2473.2 eV for **2** and is shifted by 0.2 eV upon oxidation to **2**^{ox} (2473.4 eV). This is again in good agreement with a metal-centered redox process supporting the $[Fe^{IV}(Et_2dtc)(mnt)_2]^-$ description for **10**^{ox}. Three pseudo-Voigt peaks were needed to obtain a satisfactory fit of the experimental data in the pre-edge region for both compounds. The assignment of these features is not possible without a careful theoretical analysis, because the two different sulfur donor ligands give rise to a separate set of transitions not resolved in the experimental spectrum. Therefore, a more detailed discussion of the pre-edge region is provided in the TD-DFT section.

Figure S8 (Supporting Information) shows the deconvoluted S K-edge spectra of **3** and **3**^{ox}. Similar to **2** and **2**^{ox} the pre-edge region was fitted with three pseudo-Voigt peaks and a detailed analysis is provided in the TD-DFT section. The edge feature is observed at 2473.5 and 2473.6 eV for **3** and **3**^{ox}, respectively. Again the small shift of 0.1 eV indicates a metal-centered redox process supporting an oxidation state of +IV of the central Fe ion in **3**^{ox}.

DFT calculations: The geometry optimizations of the structures of compounds **1**–**4** and **1**^{ox}–**4**^{ox} were performed at the BP86 level of DFT. The obtained structural parameters are in excellent agreement with the experimental data (see Table S5 in the Supporting Information). The calculated intraligand bond distances are within ±0.02 Å of the experimental values. The calculated Fe–S bond lengths are overestimated by up to 0.07 Å, which is typical for modern DFT

functionals. The twist angles Θ are reproduced nicely within 5° and the general trend of a decrease in Θ upon oxidation of the complex is reproduced for all complexes. The electronic ground-state calculations on the optimized structures were carried out by using the B3LYP functional.

For complexes **1**–**4** a doublet ground state ($S=^1/_2$) was assumed for the calculations in agreement with the low-temperature magnetic susceptibility and EPR data. The spin density plots obtained from a Mulliken population analysis of **1**–**4** are shown in Figure 11. In all complexes, the unpaired electron resides almost completely on the metal center. For **1**–**3**, the spin density on the iron atom is very close to the expectation value of one unpaired electron for a low-spin Fe^{III} ion (Table 8). In **4**, strong spin-polarization of the σ bonds increases the α-spin density on the iron (1.27), whereas the sulfur atoms of the ligands carry some β-spin density (−0.35). For all four complexes, two doubly occupied orbitals and one singly occupied orbital can be found, which exhibit major contributions from the t_{2g} set (d_{xz}, d_{yz}, and $d_{x^2-y^2}$). In addition, two empty metal d orbitals can be identified representing the e_g set (d_{xy} and d_{z^2}). Consequently, **1**–**4** are best described as low-spin Fe^{III} species. As expected, the mixing between the t_{2g} and the e_g set increases with increasing trigonal distortion. However, the t_{2g}–e_g mixing is small (<10% contribution of d_{xy} and d_{z^2} to the t_{2g} orbitals).

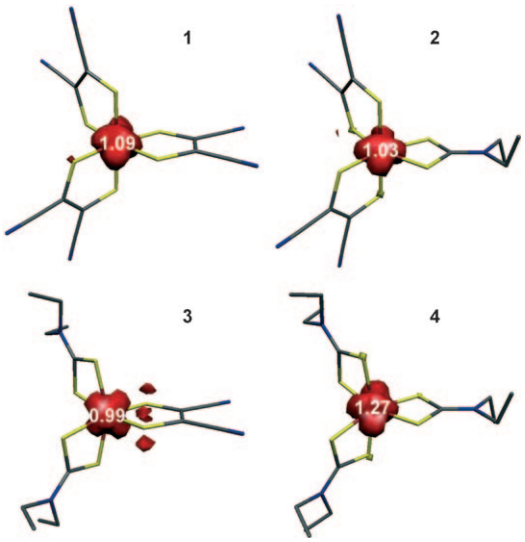

Figure 11. Mulliken spin-density plots for **1**–**4** obtained from B3LYP DFT calculations.

Table 8. Spin densities for **1**–**4** and $\mathbf{1^{ox}}$–$\mathbf{4^{ox}}$ obtained from Mulliken population analyses.

	Fe	Σ S_{mnt}	Σ C_{mnt}	Σ S_{dtc}	Σ C_{dtc}	Σ N_{dtc}
1	1.09	−0.05	−0.04	–	–	–
2	1.03	0.02	−0.02	−0.02	−0.01	0.00
3	0.99	0.11	−0.02	−0.07	−0.01	0.00
4	1.27	–	–	−0.31	0.02	0.02
$\mathbf{1^{ox}}$	1.77	0.27	−0.03	–	–	–
$\mathbf{2^{ox}}$	1.59	0.47	0.01	−0.06	−0.01	0.00
$\mathbf{3^{ox}}$	1.77	0.35	0.05	−0.02	0.01	0.03
$\mathbf{4^{ox}}$	2.33	–	–	−0.45	0.03	0.09

For the one-electron oxidized species $\mathbf{1^{ox}}$–$\mathbf{4^{ox}}$, two different electronic structures were considered to describe the triplet ground state determined experimentally. A simple spin-unrestricted approach with a multiplicity of three ($S=1$) was used to model a low-spin Fe^{IV} center with three closed-shell ligands, whereas the possibility of a ligand radical antiferromagnetically coupled to an intermediate-spin Fe^{III} ion was taken into account by a broken-symmetry, BS(3,1), approach. In all cases, the broken-symmetry calculations converged back to the simple unrestricted triplet ground state ($S=1$). Consistent with the Fe^{IV} description, one doubly occupied and two singly occupied metal d orbitals (t_{2g} set) are found in addition to two unoccupied e_g orbitals.

The spin density plots for $\mathbf{1^{ox}}$–$\mathbf{4^{ox}}$ are shown in Figure 12 and the atomic contributions to the total spin density are shown in Table 8. For all compounds, the spin density at the iron center is close to the expectation value of a low-spin Fe^{IV} (two unpaired electrons). Thus, an intermediate-spin Fe^{III} state with three unpaired electrons can unambiguously be excluded.

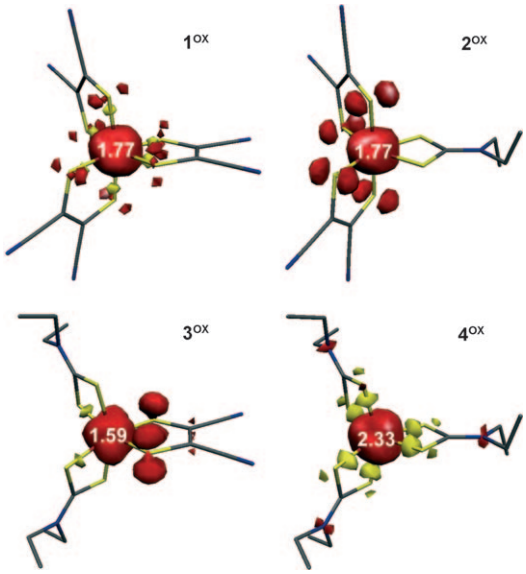

Figure 12. Mulliken spin-density plots for $\mathbf{1^{ox}}$–$\mathbf{4^{ox}}$ obtained from B3LYP DFT calculations.

However, for the mnt-containing complexes $\mathbf{1^{ox}}$–$\mathbf{3^{ox}}$, the spin density at the Fe ion is significantly lower than 2.00, whereas $\mathbf{4^{ox}}$ shows an increased value of 2.33. These deviations are accounted for by covalent interactions between the metal and the ligands. While the strong π donor $(mnt)^{2-}$ reduces the spin density at the metal ion by interaction with the t_{2g} SOMOs, σ donation into the empty e_g orbitals by the $(Et_2dtc)^{1-}$ ligand increases the spin density at the metal center due to strong exchange interactions at the paramagnetic metal center, which causes significant spin polarization

of the σ bonds. Consequently, the $(mnt)^{2-}$ ligands carry small amounts of positive spin density in π-type orbitals, whereas the $(Et_2dtc)^{1-}$ ligands exhibit some negative spin density in σ type orbitals. The presence of significant covalent contributions in all complexes **1^{ox}**–**4^{ox}** suggests that covalency plays an important role in the stabilization of the high-valent Fe^{IV} center.

The Mössbauer parameters shown in Table 9 were calculated based on the computed electronic structures. The calculated isomer shifts are in excellent agreement

Table 9. Comparison of the calculated and experimental (in parentheses) Mössbauer parameters.

	δ [mm s^{-1}]		ΔE_Q [mm s^{-1}]		η[a]	
1	0.37	(0.36)	+1.90	(−1.68)	0.98	(0.85)
2	0.38	(0.39)	−2.35	(−1.77)	0.65	(0.62)
3	0.41	(0.41)	−2.05	(−1.82)	0.77	(0.71)
4	0.51	(0.47)	+1.67	(−0.70)	0.48	(0.05)
1^{ox}	0.22	(0.24)	−2.03	(−1.56)	0.05	(0.14)
2^{ox}	0.24	(0.25)	−2.05	(−1.70)	0.98	(0.85)
3^{ox}	0.28	(0.28)	+2.07	(+1.98)	0.86	(0.70)
4^{ox}	0.28	(0.30)	−2.85	(2.48)[b]	0.11	–[c]

[a] Asymmetry parameter of the electric field gradient. [b] Sign not experimentally determined. [c] Not experimentally determined.

(±0.04 mm s^{-1}) with the experimental ones. For compounds **1**–**3** and **1^{ox}**–**3^{ox}**, the calculated quadrupole splittings are in good agreement with the experimental parameters. Even the sign of the quadrupole splitting and the asymmetry parameter of the electric field gradient, η, obtained from magnetic Mössbauer measurements are correctly predicted. For **1**, the calculated η of 0.98 indicates that the field gradient possesses two major components of opposite sign, such that the sign is irrelevant. Therefore, the agreement between calculation and experiment for **1** is excellent. For **4**, the correlation between calculated and experimental quadrupole splitting is poor. This is again due to the particular electronic structure with two nearly degenerate t_{2g} orbitals occupied by three electrons. This configuration yields large orbital contributions to the electric field gradient by spin-orbit coupling, which is not included in the computational method.

TD-DFT calculations: TD-DFT calculations of the pre-edge transitions in S K-edge spectroscopy were performed at the BP86 level for **1**–**4** and **1^{ox}**–**4^{ox}**. The sulfur donor atoms in these compounds cannot be treated as equivalent, since they are not related by symmetry. Therefore, the transitions from each of the six sulfur 1s orbitals were calculated separately. Due to the higher symmetry of the homoleptic complexes, only small differences in the obtained transition energies were observed, which are about one order of magnitude smaller than the theoretical line width of 0.8 eV. Hence, the six sulfur atoms were considered equivalent for the analysis of the transitions. For the heteroleptic complexes, three pairs of equivalent sulfur atoms were found, which reflect the symmetry related sulfur atoms in idealized octahedral geometry (Scheme 2). The influence of the observed distortions of the octahedral symmetry (see above) on the S 1s orbitals is negligible.

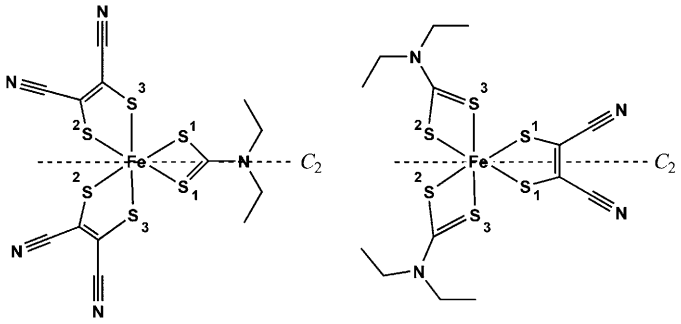

Scheme 2. Representation of the symmetry-equivalent sulfur atoms in **2**/**2^{ox}** (left) and **3**/**3^{ox}** (right) assuming idealized octahedral symmetry of the FeS_6 octahedron.

A comparison of the calculated pre-edge region of the S K-edge spectra with the experimental data is shown in Figures 13 and S9 (Supporting Information). The theoretical spectrum is a normalized superposition of the six individually calculated S spectra. Note, that the normalization factor for all calculated spectra was identical, which allows the comparison of the calculated intensities within the series. The calculated spectra reproduce all the key features of the experimental spectra.

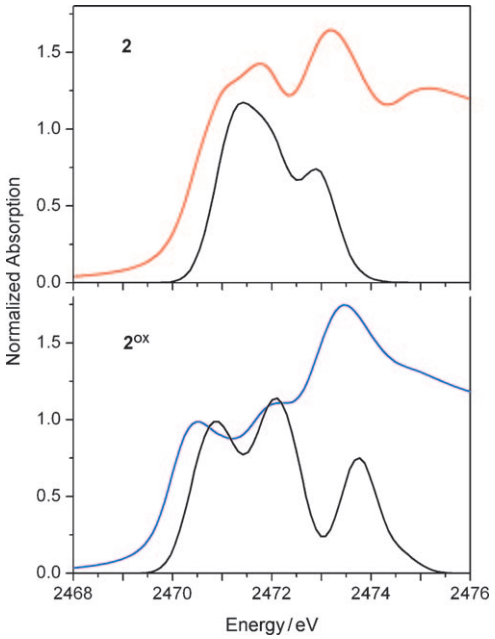

Figure 13. Comparison of the calculated (——) and experimental (—— and ——) S K-edge XAS spectra of **2** and **2^{ox}**. A line broadening of 1 eV was assumed for the calculated spectrum.

The analysis of the calculated transitions yields very similar results for all seven spectra. As a representative example, the transition analysis for the three independent sulfur atoms in **2^{ox}** is shown in Figure 14 and Table 10. The detailed

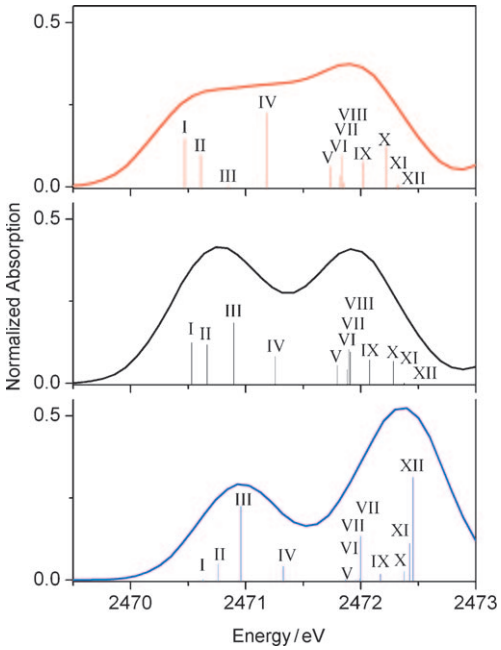

Figure 14. Calculated pre-edge transitions of the three nonequivalent sulfur atoms in **2**^{ox}. The numbers refer to the numbering scheme shown in Scheme 2. The transitions can be assigned consecutively as I–XII by starting from the left for each of the three independent sulfur atoms (——: S mnt_{cis} (3), ——: S mnt_{trans} (2), and ——: S Et_2dtc (1)).

Table 10. Calculated transition energies and oscillator strengths, f_{osc}, for the three different sulfur atoms in **2**^{ox}.

Transition	S Et_2dtc (1)		S mnt_{trans} (2)		S mnt_{cis} (3)	
	energy [eV]	$f_{osc}\times10^4$	energy [eV]	$f_{osc}\times10^4$	energy [eV]	$f_{osc}\times10^4$
I β–t_{2g}	2470.63	0.08	2470.53	3.99	2470.47	4.66
II β–t_{2g}	2470.76	1.56	2470.67	3.80	2470.61	3.09
III α–e_g	2470.96	7.20	2470.90	5.92	2470.85	0.12
IV α–e_g	2471.32	1.37	2471.26	2.63	2471.19	7.18
V α–mnt π*	2471.86	0.04	2471.80	1.77	2471.74	2.00
VI α–mnt π*	2471.95	0.01	2471.88	1.32	2471.83	1.05
VII β–mnt π*	2471.99	0.13	2471.90	3.31	2471.84	3.05
VIII β–e_g	2471.99	4.29	2471.91	3.08	2471.86	0.40
IX β–mnt π*	2472.17	0.60	2472.08	2.29	2472.02	2.45
X β–e_g	2472.37	0.87	2472.28	2.19	2472.22	3.90
XI α–Et_2dtc π*	2472.42	3.59	2472.38	0.03	2472.32	0.14
XII β–Et_2dtc π*	2472.45	10.04	2472.38	0.01	2472.32	0.13

analysis for the remaining compounds can be found in the Supporting Information (Figures S10–S15 and Tables S6–S11).

For each of the three independent (i.e. not symmetry equivalent) sulfur atoms in **2**^{ox}, twelve transitions (labeled with the Roman numerals I–XII) can be identified in the calculated pre-edge region. The first peak is the result of transitions to the SOMOs of the t_{2g} set (I and II) and the α–e_g orbitals (III and IV), whereas the second peak contains transitions to the ligand π* orbitals and to the β–e_g transitions (VIII and X). The intensities of the transitions depend on the overlap integral of the S 1s donor orbital with the acceptor orbitals of the transitions, which are shown in Figure 15. Therefore, the intensities for transitions from the Et_2dtc sulfur atoms (1) to the mnt π* orbitals are small and vice versa. In agreement with the ligand field model described (vide infra), the SOMOs of **10**^{ox} are two t_{2g} orbitals, which are destabilized by π donation of the mnt ligands. Consequently, the overlap between these metal orbitals and the mnt π* orbitals is large and results in high intensities of the transitions I and II for the mnt sulfur atoms (2 and 3). In contrast, the same transitions for the Et_2dtc sulfur atoms (1) exhibit much smaller intensities.

Following this analysis, the twelve transitions found for each independent sulfur atom in the Fe^{IV} complexes **1**^{ox}–**3**^{ox} can be arranged in four different groups:

1) Two β-spin transitions into the half-filled t_{2g} orbitals.
2) Two α-spin transitions into the empty eg set.
3) Two β-spin transitions into the empty eg set.
4) Three α- and three β-spin transitions into the empty ligand π* orbitals.

Note that the transitions to the empty metal d orbitals are multiplet split (~1 eV) due to the paramagnetic metal center.

The energy differences between the transitions are too small to allow the observation of well resolved peaks for each transition in the spectra. The transitions to the t_{2g} set (1) occur in the same energy region as the α–e_g transitions (2), giving rise to the first experimentally observed pre-edge peak. Likewise, the β–e_g transitions (3) occur at comparable energies with the transitions to the ligand π* (4) constituting the second pre-edge feature in the spectrum. Generally, the transitions to the π* orbital of Et_2dtc occur at slightly lower energies than the corresponding mnt transitions, which is consistent with the experimental values for the free ligands.

For the Fe^{III} complexes **1**–**4**, one more electron is found in the t_{2g} set. Therefore, only eleven transitions are found in the pre-edge region for each independent sulfur atom. Besides the reduced peak number, two major differences between the Fe^{III} series and the Fe^{IV} complexes can be observed by analyzing the calculated spectra. Firstly, the multiplet splitting of the e_g transitions is smaller for the Fe^{III} complexes (~0.5 eV), in agreement with the reduced total spin of the compounds. Secondly, two resolved pre-edge peaks are observed for **1**^{ox}–**3**^{ox}, whereas the two peaks are merged for **1**–**4**. This is consistent with a metal-centered redox process. Due to the higher Z_{eff} of the Fe^{IV} ion, the d orbital manifold is stabilized and lowered in energy. Therefore, the first pre-edge peak, consisting of transitions to the t_{2g} and α–e_g set, shifts to lower energy in **1**^{ox}–**3**^{ox}. Most significantly, evidence for the absence of ligand

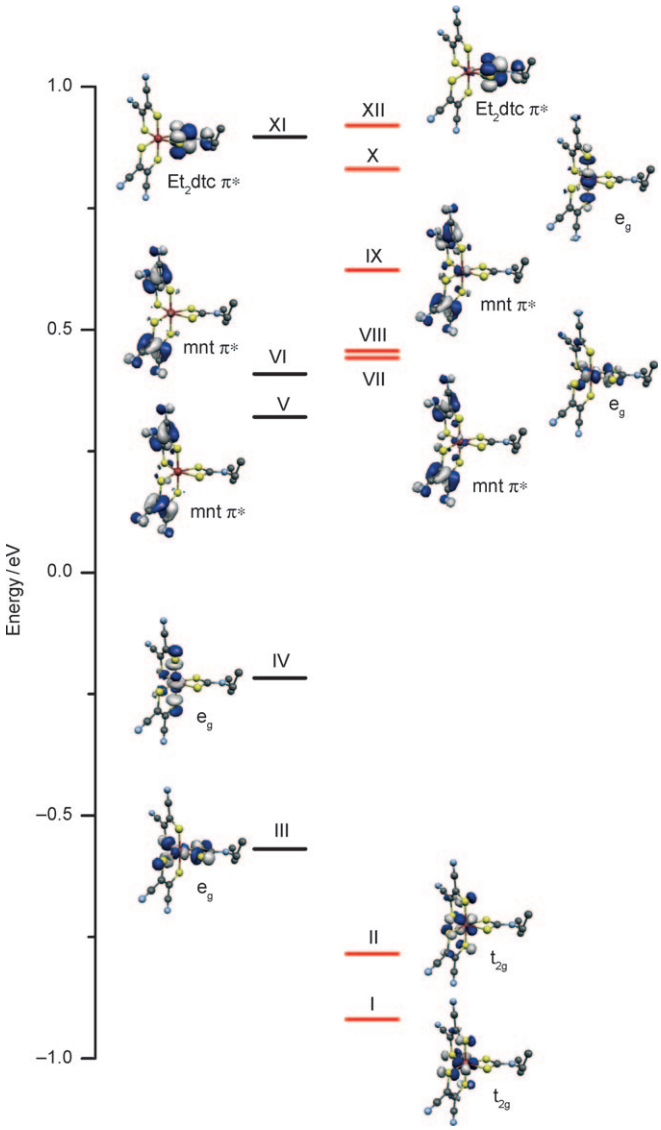

Figure 15. Acceptor orbitals (——: α-spin, ——: β-spin) of the first twelve transitions (indicated by Roman numerals) in the calculated S K-edge spectrum of **2^{ox}**.

radicals in all complexes is provided by the fact that none of the acceptor orbitals exhibits predominant ligand π* character. However, both the t_{2g} and the e_g acceptor orbitals show significant contributions from ligand orbitals (>25%) reflected in the high intensities of the transitions and consistent with a highly covalent bonding situation.

In summary, the TD-DFT calculations of the S K-pre-edge spectra present a powerful tool for the analysis of the complex transition patterns in this region. The analysis of the calculated pre-edge transitions confirms the Fe^{IV} description, but also indicates strong ligand-to-metal σ and π donation resulting in very covalent bonding. This ties in nicely with the spin-density analysis from DFT calculations and the trends observed in the Mössbauer parameters.

Discussion

In this section we will develop a simple ligand-field model to understand the observed trends in the EPR and Mössbauer spectra in conjunction with the structural data for the ferric complexes **1**–**4** and their one-electron oxidized species **1^{ox}**–**4^{ox}**. In perfect octahedral geometry both low-spin ferric and low-spin Fe^{IV} species possess an orbitally degenerate ground state with five and four 3d electrons distributed over three t_{2g} metal d orbitals, respectively, as shown in Figure 16. According to the Jahn–Teller theorem this represents an unstable, energetically degenerate configuration that will undergo distortions lifting the degeneracy. It is, therefore, important to analyze the impact of different structural motifs on the energy splitting of the t_{2g} orbitals.

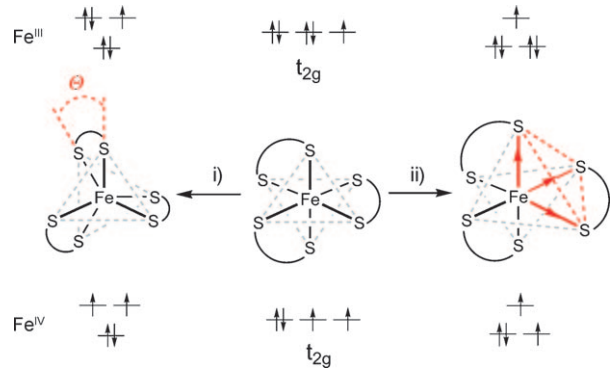

Figure 16. i) Influence of the trigonal twist Θ on the t_{2g} orbitals of six-coordinate low-spin $Fe^{III/IV}$. ii) Splitting of the t_{2g} orbitals as a result of a trigonal elongation.

A major difference between mnt^{2-} and Et_2dtc^- is the bite angle of the ligand, which is significantly smaller for Et_2dtc^- because it forms only four-membered chelate rings in contrast to the five-membered rings of the M–mnt^{2-} unit. The normalized ligand bite b of the chelate ligand, which is defined as the distance between the donor atoms of the chelate divided by the metal–ligand bond length, influences the trigonal twist Θ along the approximate C_3 axis of the compounds. The smaller normalized bite of Et_2dtc^- gives rise to small values for Θ and thus large deviations from octahedral geometry. Therefore, the trend of decreasing values of Θ_{av} within the two series **1**–**4** and **1^{ox}**–**4^{ox}** can be attributed entirely to the steric effects imposed by the geometry of the ligands. However, the decreasing Θ_{av} values upon oxidation cannot be explained by this effect. Since the Fe–S bond lengths decrease upon oxidation for all compounds while the ligand parameters remain almost unchanged, b increases, which should lead to more octahedral geometries. The opposite is observed.

The consequences of the trigonal twist on the electronic structure can be studied best in the homoleptic complexes **1**/**1^{ox}** and **4**/**4^{ox}**, because all six donor atoms of the ligands are equivalent and the t_{2g} set is not split by an inhomogeneous ligand environment. Therefore all ligand-field splittings

within this set must arise from distortions of the octahedral geometry. The principal ligand-field splitting of the metal d orbitals caused by the trigonal twist Θ going from octahedral to trigonal prismatic geometry is shown in Figure 17. In-

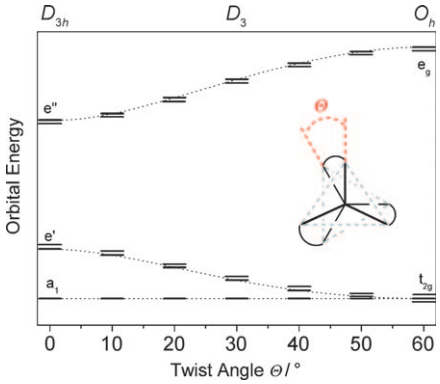

Figure 17. Correlation diagram depicting the effect of the trigonal twist on the energy of the metal d orbitals.

creasing the trigonal distortion mixes the t_{2g} and e_g orbitals and splits the t_{2g} set into an a_1 orbital and an e' set. Furthermore, the energy difference between the former t_{2g} and e_g orbitals decreases. Note that the trigonal twist decreases the ligand-field stabilization energy for both low-spin d^5 and d^4 systems and is, therefore, unfavorable in the ligand-field framework. However, it has been suggested for dithiolene complexes that the trigonal distortion enhances stabilizing π interactions.[34] Figure 16 shows that the trigonal twist leads to an orbitally nondegenerate ground state for the low-spin Fe^{IV} systems. In contrast, the low-spin Fe^{III} configuration still exhibits degeneracy. Therefore, the smaller Θ found for $\mathbf{1}^{ox}$ and $\mathbf{4}^{ox}$ relative to their Fe^{III} analogues can be interpreted as a Jahn–Teller distortion, whereas the small twists in **1** and **4** result from the ligand bite and are in fact close to the octahedral limit[26] for mnt^{2-} and Et_2dtc^-, respectively.

For **1** a second distortion described as a trigonal elongation resulting from a lengthening of the Fe–S bonds associated with the S(1), S(4), and S(14) face, is depicted in Figure 16. This distortion results in an orbitally nondegenerate ground state for low-spin Fe^{III}, but not for Fe^{IV}. Consistent with this is the fact that the trigonal elongation is not observed in $\mathbf{1}^{ox}$. For **4**, the expected trigonal elongation is not observed in the crystal structure, which might be the result of a dynamic Jahn–Teller distortion averaging the observed bond distances. Additionally, the rigidity of the Et_2dtc^- four-membered chelate ring possibly restricts the magnitude of the distortion.

The combination of the two different trigonal distortions yields quite different electronic structures for **1** and **4**, as is most clearly detected in their EPR spectra. A comparison of their disparate ligand-field splitting patterns is shown in Figure 18a. For **1**, the large trigonal elongation is the dominating ligand-field effect, which isolates the unpaired electron in one d orbital. The additional, sterically enforced twist is small, but leads to a further splitting of the remaining two

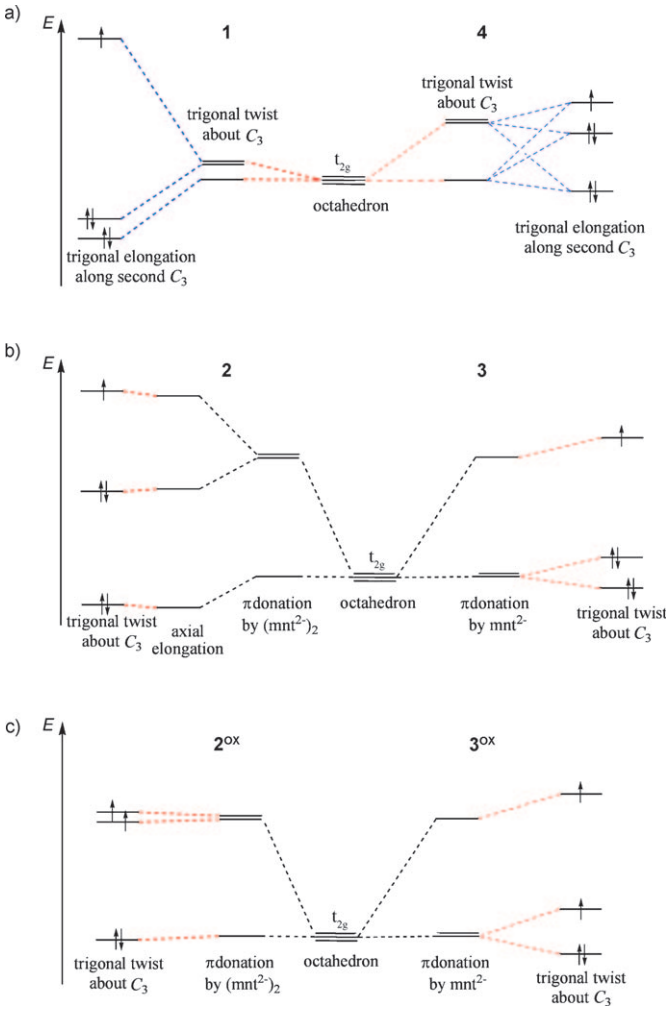

Figure 18. Qualitative ligand-field splitting diagram of the t_{2g} orbitals in a) **1** (left) and **4** (right), b) **2** (left) and **3** (right), c) $\mathbf{2}^{ox}$ (left) and $\mathbf{3}^{ox}$ (right).

doubly-filled orbitals giving a rhombic spectrum. If these two orbitals were degenerate, the resulting spectrum would be axial. In contrast, the dominating effect in **4** must be the stronger trigonal twist enforced by the Et_2dtc^- ligands. It yields a degenerate ground state with five electrons in a "two-over-one" orbital set, which is further split by a small trigonal elongation resulting in the rhombic HALS EPR spectrum.

For the heteroleptic complexes $\mathbf{2}/\mathbf{2}^{ox}$ and $\mathbf{3}/\mathbf{3}^{ox}$ the ligand-field splitting is dominated by the different donor properties of the ligands. In contrast to dithiocarbamates, dithiolenes such as mnt^{2-} are very strong π donors, as deduced from the Mössbauer quadrupole splittings (see above). Therefore, they destabilize the metal π orbitals (the t_{2g} set in octahedral compounds), which are no longer nonbonding, but antibonding with respect to the ligand.

In **2** and $\mathbf{2}^{ox}$ two of the t_{2g} orbitals are destabilized by the two mnt^{2-} ligands. For the d^5 system in **2**, this yields an orbitally degenerate ground state, which is further split by an axial elongation in agreement with the Jahn–Teller theorem. For **3**, only one orbital is destabilized resulting in a nonde-

generate ground state. Consequently, no further distortion is observed apart from the enforced trigonal twist (Figure 18b).

For **2^{ox}**, the orbital splitting by the heterogeneous ligand environment already yields a nondegenerate ground state for low spin Fe^{IV}. Therefore, no further distortion is necessary and the axial distortion observed in **2** is absent in **2^{ox}**. Additionally, the increase in Θ_{av} upon oxidation is smaller (1.8°) than for the other members of the series. In contrast, the trigonal twist is essential to create a nondegenerate ground state in **3^{ox}**, depicted in Figure 18c.

Conclusion

This work presents the first comparative study of the ferric complexes $[Fe(Et_2dtc)_{3-n}(mnt)_n]^{n-}$ (**1**–**4**, $n=3$, 2, 1, 0) and their corresponding one-electron oxidized species $[Fe(Et_2dtc)_{3-n}(mnt)_n]^{(n-1)-}$ (**1^{ox}**–**4^{ox}**). The detailed experimental and quantum chemical investigation suggests that the oxidized species are best viewed as genuine low-spin Fe^{IV} complexes (d^4, $S=1$). This is in stark contrast to the previously reported diamagnetic complex $[Fe^{III}(cyclam)(mnt^{\bullet})]^{2+}$, in which an $(mnt^{\bullet})^{1-}$ ligand π radical is intramolecularly antiferromagnetically coupled to a low-spin ferric ion. The theoretical data indicate that the Fe–S bonds in **1^{ox}**–**4^{ox}** are highly covalent, which facilitates the stabilization of the unusually high oxidation state of +IV. This is particularly true for the strong π donor $(mnt)^{2-}$ that forms very covalent π bonds with the t_{2g} orbitals of the metal and allows for some delocalization of the charge. However, we found no experimental or computational evidence for ligand oxidation to $(mnt^{\bullet})^{1-}$ resulting in broken-symmetry states for **1^{ox}**–**3^{ox}**. Based on their electronic structures we have also developed a simple ligand-field picture correlating the geometric features of the complexes with their spectroscopic properties.

Experimental Section

Preparation of complexes: The complexes **1**, **1^{ox}**, **2**, **3**, and **4** have been prepared by following literature procedures. Single crystals of **1**, **1^{ox}**, and **4** were grown by slow evaporation of concentrated CH_2Cl/EtOH solutions. Crystals of **2** and **3** were isolated after slow evaporation of concentrated MeOH/H_2O and CH_2Cl_2/MeOH solutions, respectively.

$(PPh_4)[Fe^{IV}(Et_2dtc)(mnt)_2]$ ((PPh_4)2^{ox}): Solid ferrocenium hexafluorophosphate (28 mg, 0.086 mmol) was added to a solution of $(PPh_4)_2[Fe^{III}(Et_2dtc)(mnt)_2]$ (100 mg, 0.086 mmol) in dichloromethane (25 mL) under an argon blanketing atmosphere. After stirring for 1 h at room temperature, hexane (20 mL) was added. A white precipitate formed that was filtered off in air. Upon evaporation of the dichloromethane from the filtrate, a black powder precipitated, which was filtered and washed with hexane. The powder was redissolved in an acetonitrile/water mixture (3:1). Upon slow evaporation of the solvent, crystals of the product were obtained as black needles. These were filtered, washed with water, and dried in air. Yield: 52 mg (73%); elemental analysis calcd (%) for $C_{37}H_{30}FeN_5PS_6$: C 53.94, H 3.67, N 8.50, Fe 6.78; found: C 54.15, H 3.73, N 8.43, Fe 6.65.

$[Fe^{IV}(Et_2dtc)_2(mnt)]$ (3^{ox}): Solid ferrocenium hexafluorophosphate (53 mg, 0.16 mmol) was added to a solution of $(Et_4)[Fe^{III}(Et_2dtc)_2(mnt)]$ (100 mg, 0.16 mmol) in dichloromethane (25 mL) under an argon blanketing atmosphere. After stirring for 1 h at room temperature, hexane (10 mL) was added. Upon slow evaporation of the solvent, crystals of the product were obtained as fine black needles. These were filtered, washed with hexane, and dried in air. Yield: 75 mg (95%); elemental analysis calcd (%) for $C_{14}H_{20}FeN_4S_6 \cdot {}^1/_4\,CH_2Cl_2$: C 33.31, H 4.02, N 10.90, Fe 10.87; found: C 33.50, H 4.01, N 10.88, Fe 10.78.

X-ray crystallographic data collection and refinement of the structures (Table 11): Dark-red single crystals of 1·CH_2Cl_2 and **3**, and black crystals of **1^{ox}**, **2**, **2^{ox}**, **3^{ox}**, and **4** were coated with perfluoropolyether, picked up with nylon loops and mounted in the nitrogen cold stream of the diffractometers equipped with a Mo-target rotating-anode X-ray source. Graphite monochromated $Mo_{K\alpha}$ radiation ($\lambda=0.71073$ Å) was used throughout. Final cell constants were obtained from least-squares fits of several thou-

Table 11. Crystallographic data for 1·CH_2Cl_2, **1^{ox}**, **2**, **2^{ox}**, **3**, **3^{ox}**, and **4**.

	$(PPh_4)_3$**1**·CH_2Cl_2	$(PPh_4)_2$**1^{ox}**	$(PPh_4)_2$**2**	(PPh_4)**2^{ox}**	(NEt_4)**3**	**3^{ox}**	**4**
chemical formula	$C_{85}H_{62}Cl_2FeN_6P_3S_6$	$C_{60}H_{40}FeN_6P_2S_6$	$C_{61}H_{50}FeN_5P_2S_6$	$C_{37}H_{30}FeN_5PS_6$	$C_{22}H_{40}FeN_5S_6$	$C_{14}H_{20}FeN_4S_6$	$C_{15}H_{30}FeN_3S_6$
crystal size, [mm^3]	0.06×0.02×0.02	0.08×0.08×0.02	0.20×0.18×0.12	0.13×0.11×0.11	0.04×0.03×0.02	0.28×0.07×0.06	0.06×0.03×0.02
F_w	1579.43	1155.13	1163.21	823.84	622.80	492.55	500.63)
space group	$P2_1/c$, no. 14	*Pbcn*, no. 60	*Pbcn*, no. 60	*Pn*, no. 7	$P\bar{1}$, no. 2	$P2_12_12_1$, no. 19	*C2/c*, no. 15
a [Å]	24.450(2)	19.9180(6)	20.4285(6)	14.0152(6)	9.780(2)	9.9133(9)	13.9877(10)
b [Å]	14.5135(14)	15.4386(4)	15.2892(5)	7.4610(3)	10.254(2)	12.9464(15)	10.2196(8)
c [Å]	24.573(3)	17.8738(6)	17.8309(5)	18.6852(9)	15.869(3)	16.325(2)	16.9229(12)
α [°]	90	90	90	90	90.047(4)	90	90
β [°]	116.959(12)	90	90	92.107(2)	90.389(4)	90	110.559(6)
γ [°]	90	90	90	90	110.194(4)	90	90
V [Å^3]	7772.4(13)	5496.3(3)	5569.2(3)	1952.5(2)	1493.6(8)	2095.2(4)	2265.0(3)
Z	4	4	4	2	2	4	4
T [K]	100(2)	100(2)	100(2)	100(2)	100(2)	100(2)	100(2)
ρ_{calcd} [g cm^{-3}]	1.350	1.396	1.387	1.401	1.385	1.561	1.468
refl. collected/$2\Theta_{max}$	210205/60.00	64562/50.00	94677/62.00	69036/70.00	100278/60.00	43773/64.98	11333/60.00
unique refl./$I>2\sigma(I)$	22628/16217	4819/3689	8866/6735	16871/14922	8717/6753	7564/6249	3029/2310
no. of params/restr.	938/3	339/0	341/0	453/2	315/0	253/21	124/2
λ [Å]/$\mu_{(K\alpha)}$ [cm^{-1}]	0.71073/5.35	0.71073/6.07	0.71073/5.98	0.71073/7.82	0.71073/9.45	0.71073/13.24	0.71073/12.24
$R1$[a]/GooF[b]	0.0412/1.034	0.0368/1.040	0.0373/1.023	0.0314/1.018	0.0319/1.084	0.0478/1.028	0.0422/1.023
$wR2$[c] ($I>2\sigma(I)$)	0.0854	0.0658	0.0807	0.0669	0.0669	0.01107	0.0877
residual density [eÅ^{-3}]	+0.98/−1.07	+0.32/−0.29	+0.41/−0.66	+0.31/−0.46	+0.51/−0.45	+1.13/−1.03	+0.71/−0.81

[a] Observation criterion: $I>2\sigma(I)$ $R1=\Sigma||F_o|-|F_c||/\Sigma|F_o|$. [b] $GooF=[\Sigma[w(F_o^2-F_c^2)^2]/(n-p)]^{1/2}$. [c] $wR2=[\Sigma[w(F_o^2-F_c^2)^2]/\Sigma[w(F_o^2)^2]]^{1/2}$, in which $w=1/\sigma^2(F_o^2)+(aP)^2+bP$, $P=(F_o^2+2F_c^2)/3$.

sand strong reflections. Intensities of redundant reflection were used to correct for absorption by using the program SADABS.[35] The structures were readily solved by Patterson methods and subsequent difference Fourier techniques. The Siemens ShelXTL[36] software package was used for the solution and artwork of the structures, ShelXL97[37] was used for the refinement. All non-hydrogen atoms were anisotropically refined and hydrogen atoms were placed at calculated positions and refined as riding atoms with isotropic displacement parameters.

The CH_2Cl_2 molecule in **1**·CH_2Cl_2 was found to be disordered. Two split positions were refined in an about 90:10 ratio. Anisotropic displacement parameters and bond distances of corresponding disordered atoms were restrained by using the EADP and SAME instruction of ShelXL. A disordered dithiocarbamate ligand in $\mathbf{3}^{ox}$ (S11 to C18) was treated the same way. SAME and EADP instructions were used to yield two equally occupied positions of the ligand. Some disorder was also detected in **4**, in which an ethyl group of diethyldithiocarbamate (C17 and C18) was refined on two positions giving an occupation ratio of about 0.86:0.14. Crystallographic data of the compounds are listed in Table 1.

CCDC-727021, 727022, 727023, 727024, 727025, 727026, and 727027 contain the supplementary crystallographic data for this paper. These data can be obtained free of charge from The Cambridge Crystallographic Data Centre via www.ccdc.cam.ac.uk/data_request/cif

Physical measurements: Elemental analyses were measured at the Mikroanalytisches Labor H. Kolbe, in Mülheim an der Ruhr (Germany). Cyclic voltammograms were recorded at 25 °C by using an EG&G Potentiostat/Galvanostat 273A. A three-electrode cell was employed with a glassy-carbon working electrode, a glassy-carbon auxiliary electrode, and a $Ag/AgNO_3$ reference electrode (0.01 M $AgNO_3$ in CH_3CN). Ferrocene was added as an internal standard after completion of the measurements, and potentials are referenced versus the Fc^+/Fc couple. Controlled potential coulometric measurements were performed in a setup that allows recording of absorption spectra in situ during electrolysis by employing the same potentiostat, but using a Pt-grid as a working electrode. A Pt-brush was used as counter electrode and separated from the working electrode compartment by a Vycor frit. An $Ag/AgNO_3$ (0.01 M $AgNO_3$ in CH_3CN) reference electrode was employed again. UV/Vis spectra were measured on a Perkin–Elmer UV/Vis Lambda 19 spectrophotometer (250–200 nm). Temperature-dependent magnetic susceptibilities were measured by using a SQUID magnetometer (MPMS Quantum Design) at 1.0 T (4–300 K). Underlying diamagnetism was corrected by using tabulated Pascal's constants. X-band EPR derivative spectra were recorded on a Bruker ELEXSYS E500 spectrometer equipped with the Bruker standard cavity (ER4102ST) and a helium flow cryostat (Oxford Instruments ESR 910). Microwave frequencies were calibrated with a Hewlett–Packard frequency counter (HP5352B), and the field control was calibrated with a Bruker NMR field probe (ER035 M). The spectra were simulated with the program GFIT (by Eckhard Bill) for the calculation of powder spectra with effective g values and anisotropic line widths (Gaussian line shapes were used). Mössbauer data were recorded on a spectrometer with alternating constant acceleration. The minimum experimental line width was 0.24 $mm\,s^{-1}$ (full width at half-height). The sample temperature was maintained constant either in an Oxford Instruments Variox or an Oxford Instruments Mössbauer-Spectromag cryostat. The latter is a split-pair super-conducting magnet system for applied fields up to 8 T in which the temperature of the sample can be varied in the range of 1.5–250 K. The field at the sample is perpendicular to the γ-beam. Isomer shifts are quoted relative to iron metal at 300 K. Magnetic Mössbauer spectra were simulated with the program MX (by Eckhard Bill).

X-ray absorption spectroscopy measurements and data analysis: All data were measured at the Stanford Synchrotron Radiation Laboratory under the ring conditions of 3.0 GeV and 60–100 mA. All S K-edge data were measured by using the 54-pole wiggler beam line 6–2 in the high magnetic field mode of 10 kG with a Ni-coated harmonic rejection mirror and a fully tuned Si(111) double-crystal monochromator. Details of the optimization of this setup have been previously described. Data were measured at room temperature by fluorescence, with a Lytle detector. To check for reproducibility, two to three scans were measured for each sample. The energy was calibrated from S K-edge spectra of $Na_2S_2O_3{\cdot}5H_2O$, run at intervals between sample scans. The maximum of the first pre-edge feature in the spectrum was fixed at 2472.02 eV. A step size of 0.08 eV was used over the edge region. Data were averaged and a smooth background was removed from all spectra by fitting a polynomial to the pre-edge region and subtracting this polynomial from the entire spectrum. Normalization of the data was accomplished by fitting a flattened polynomial or straight line to the post-edge region (2490–2740 eV) and normalizing the post-edge at 1.0.

Fe K-edge XAS data were measured on focused 16-pole wiggler beam line 9–3. A Si(220) monochromator was utilized for energy selection. A Rh-coated harmonic rejection mirror set to a 10 keV cutoff was used to minimize higher harmonics. All samples were prepared as solids in boron nitride, pressed into a pellet, and sealed between 38 μm Kapton tape windows in a 1 mm aluminum spacer. The samples were maintained at 10 K during data collection by using an Oxford Instruments CF1208 continuous flow liquid helium cryostat. Data were measured in transmission mode. Internal energy calibrations were performed by simultaneous measurement of an Fe reference foil placed between a second and third ionization chamber. The first inflection point was assigned to 7111.2 eV for Fe. Data represent three to five scan averages and were processed by fitting a second-order polynomial to the pre-edge region and subtracting this background from the entire spectrum. A three-region cubic spline was used to model the smooth background above the edge. The data were normalized by subtracting the spline and normalizing the post-edge to 1.0. The spectra were deconvoluted by using the program EDG FIT.

Calculations: All DFT calculations were performed with the ORCA[38] program package. The geometry optimizations of the complexes were performed at the BP86[39,40] level of DFT. Single-point calculations on the optimized geometries were carried out by using the B3LYP[39,41] functional. This hybrid functional often gives better results for transition-metal compounds than pure gradient-corrected functionals, especially with regard to metal–ligand covalency.[42] The all-electron Gaussian basis sets were those developed by the Ahlrichs group.[43,44] Triple-ζ quality basis sets TZV(P) with one set of polarization functions on the metals and on the atoms directly coordinated to the metal center were used.[43] For the carbon and hydrogen atoms, slightly smaller polarized split-valence SV(P) basis sets were used, that were of double-ζ quality in the valence region and contained a polarizing set of d-functions on the non-hydrogen atoms.[44] Auxiliary basis sets used to expand the electron density in the resolution-of-the-identity (RI) approach were chosen,[45] where applicable, to match the orbital basis. The SCF calculations were tightly converged ($1\times10^{-8}\,E_h$ in energy, $1\times10^{-7}\,E_h$ in the density change and 1×10^{-7} in maximum element of the DIIS error vector). The geometry optimizations for all complexes were carried out in redundant internal coordinates without imposing symmetry constraints. In all cases, the geometries were considered converged after the energy change was less than $5\times10^{-6}\,E_h$, the gradient norm and maximum gradient element were smaller than 1×10^{-4} and $3\times10^{-4}\,E_h\,Bohr^{-1}$, respectively, and the root-mean square and maximum displacements of all atoms were smaller than 2×10^{-3} and 4×10^{-3} Bohr, respectively. Throughout this paper we describe our computational results by using the broken-symmetry (BS) approach by Ginsberg[46] and Noodleman.[47] Since several broken symmetry solutions to the spin-unrestricted Kohn–Sham equations may be obtained, the general notation BS(m,n)[48] has been adopted, in which m(n) denotes the number of spin-up (spin-down) electrons at the two interacting fragments. Canonical and corresponding orbitals,[49] as well as spin density plots were generated with the program Molekel.[50] Nonrelativistic single-point calculations on the optimized geometry were carried out to predict Mössbauer spectral parameters (isomer shifts and quadrupole splittings). These calculations employed the CP(PPP) basis set[51] for iron. The Mössbauer isomer shifts were calculated from the computed electron densities at the iron centers as previously described.[52] TD-DFT calculations were performed to predict the transitions in the pre-edge region of the S and Fe K-edge XAS spectra.[53] The symmetry equivalent 1s orbitals obtained from the ground-state calculations were localized by using the Pipek-Mezey criteria[54] and TD-DFT calculations at the BP86 level were performed, allowing only for excitations from the localized sulfur 1s orbitals. The basis sets were chosen to match the basis sets used for the single-point ground state calculations. The obtained S K-edge transition

energies were corrected by a constant 56.0 eV shift to align calculated spectra with experimental spectra.

Acknowledgements

We are grateful for financial support from the Fonds der Chmischen Industrie. C.M. and S.S. gratefully acknowledge the Max-Planck Society for a stipend. Portions of this research were carried out at the Stanford Synchrotron Radiation Laboratory, a national user facility operated by Stanford University on behalf of the U.S. Department of Energy, Office of Basic Energy Sciences. The SSRL Structural Molecular Biology program is supported by the National Institutes of Health, National Center for Research Resources, Biomedical Technology Program and by the Department of Energy, Office of Biological and Environmental Research.

[1] a) R. M. Golding, C. M. Harris, K. J. Jessop, W. C. Tennant, *Aust. J. Chem.* **1972**, *25*, 2567; b) K. L. Brown, R. M. Golding, P. C. Healey, K. J. Jessop, W. C. Tennant, *Aust. J. Chem.* **1974**, *27*, 2075; c) P. Banerjee, S. Sproules, T. Weyhermüller, S. DeBeer George, K. Wieghardt, *Inorg. Chem.* **2009**, *48*, 5829.

[2] E. A. Pasek, D. K. Straub, *Inorg. Chem.* **1972**, *11*, 259.

[3] R. Y. Saleh, D. K. Straub, *Inorg. Chem.* **1974**, *13*, 3017.

[4] R. D. Webster, G. A. Heath, A. M. Bond, *J. Chem. Soc. Dalton Trans.* **2001**, 3189.

[5] a) A. M. Bond, A. R. Hendrickson, R. L. Martin, J. E. Moir, D. R. Puge, *Inorg. Chem.* **1983**, *22*, 3440; b) A. M. Bond, R. Colton, Y. Ho, J. E. Moir, D. R. Mann, R. Scott, *Inorg. Chem.* **1985**, *24*, 4402; R. G. Compton, J. C. Ecklund, L. Nei, A. M. Bond, R. Colton, Y. A. Mah, *J. Electroanal. Chem.* **1995**, *385*, 249; c) J. A. Alden, A. M. Bond, R. Colton, R. G. Compton, J. C. Eklund, Y. A. Mah, P. J. Mahon, V. Tedesco, *J. Electroanal. Chem.* **1998**, *447*, 155.

[6] a) J. P. Fackler, A. Avdeef, R. G. Fischer, *J. Am. Chem. Soc.* **1970**, *92*, 6972; b) J. P. Fackler, A. Avdeef, R. G. Fischer, *J. Am. Chem. Soc.* **1973**, *95*, 774; c) A. R. Hendrickson, R. L. Martin, N. M. Rohde, *Inorg. Chem.* **1975**, *14*, 2980; d) J. A. McCleverty, N. J. Morrison, *J. Chem. Soc. Dalton Trans.* **1976**, 541.

[7] A. H. White, R. Roper, E. Kokot, H. Waterman, R. L. Martin, *Aust. J. Chem.* **1964**, *17*, 294.

[8] a) E. A. Pasek, D. K. Straub, *Inorg. Chim. Acta* **1977**, *21*, 23; b) P. C. Healy, A. H. White, *J. Chem. Soc. Dalton Trans.* **1972**, 1163; c) R. L. Martin, N. M. Rohde, G. B. Robertson, D. Taylor, *J. Am. Chem. Soc.* **1974**, *96*, 3647.

[9] C. L. Raston, A. H. White, D. Petridis, D. Taylor, *J. Chem. Soc. Dalton Trans.* **1980**, 1928.

[10] J. G. Leipoldt, P. Coppens, *Inorg. Chem.* **1973**, *12*, 2269.

[11] R. Chant, A. R. Hendrickson, R. L. Martin, N. M. Rohde, *Inorg. Chem.* **1975**, *14*, 1894.

[12] a) V. Petrouleas, D. Petridis, *Inorg. Chem.* **1977**, *16*, 1306; b) L. M. Epstein, D. K. Straub, *Inorg. Chem.* **1969**, *8*, 784; c) J. M. Fiddy, I. Hall, F. Grandjean, G. J. Long, U. Russo, *J. Phys. Condens. Matter* **1990**, *2*, 10091; d) A. Terzis, S. Filippakis, D. Mentzafos, V. Petrouleas, A. Malliaris, *Inorg. Chem.* **1984**, *23*, 334.

[13] D. Petridis, D. Niarchos, B. Kanellakopulos, *Inorg. Chem.* **1979**, *18*, 505.

[14] J. A. McCleverty, J. Locke, E. J. Wharton, *J. Chem. Soc. A* **1968**, 816.

[15] S. A. Cotton, J. F. Gibson, *Chem. Commun.* **1968**, 883.

[16] a) J. Blomquist, U. Helgeson, B. Folkesson, R. Larsson, *Chem. Phys.* **1983**, *76*, 71; b) M. Gerloch, S. F. A. Kettle, J. Locke, J. A. McCleverty, *Chem. Commun.* **1966**, 29.

[17] E. I. Stiefel, L. E. Bennet, Z. Dori, T. H. Crawford, C. Simo, H. B. Gray, *Inorg. Chem.* **1970**, *9*, 281.

[18] A. Sequeira, I. Bernal, *J. Cryst. Mol. Struct.* **1973**, *3*, 157.

[19] G. R. Lewis, I. Dance, *J. Chem. Soc. Dalton Trans.* **2000**, 3176.

[20] J. Bray, J. Locke, J. A. McCleverty, D. Coucouvanis, *Inorg. Synth.* **1972**, *13*, 187.

[21] C. Milsmann, G. K. Patra, E. Bill, T. Weyhermüller, S. DeBeer George, K. Wieghardt, *Inorg. Chem.* **2009**, *48*, 7430.

[22] J. A. McCleverty, D. G. Orchard, K. Smith, *J. Chem. Soc. A* **1971**, 707.

[23] L. H. Pignolet, R. A. Lewis, R. H. Holm, *Inorg. Chem.* **1972**, *11*, 99; L. H. Pignolet, G. S. Patterson, J. F. Weiher, R. H. Holm, *Inorg. Chem.* **1974**, *13*, 1263.

[24] J. Stach, R. Kirmse, J. Sieler, U. Abram, W. Dietzsch, R. Bottcher, L. K. Hansen, H. Vergoossen, M. C. M. Gribnau, C. P. Keijzers, *Inorg. Chem.* **1986**, *25*, 1369.

[25] K. Mereiter, A. Preisinger, *Inorg. Chim. Acta* **1985**, *98*, 71.

[26] D. L. Kepert, *Prog. Inorg. Chem.* **1977**, *23*, 1.

[27] L. Cambi, A. Cagnasso, *Atti Accad. Naz. Lincei Ci. Sci. Fis. Mat. Nut. Rend.* **1931**, *13*, 809; L. Cambi, A. Cagnasso, *Ber Dtsch. Chem. Ges. B.* **1933**, *66*, 656.

[28] G. R. Hall, D. N. Hendrickson, *Inorg. Chem.* **1976**, *15*, 607.

[29] a) S. Singhal, A. N. Garg, *Transition Met. Chem.* **2005**, *30*, 44; b) H. H. Wickman, A. M. Trozzolo, *Phys. Rev. Lett.* **1965**, *15*, 156.

[30] a) C. Migita, M. Iwaizumi, *J. Am. Chem. Soc.* **1981**, *103*, 4378; b) J. C. Salerno, J. S. Leigh, *J. Am. Chem. Soc.* **1984**, *106*, 2156.

[31] "Electron Paramagnetic Resonance in Metalloproteins": G. Palmer in *Physical Methods in Bioinorganic Chemistry* (Ed.: L. Que Jr.), University Science Books, Sausalito, **2000**, pp. 121–185.

[32] L. Duelund, H. Toftlund, *Spectrochim. Acta Part A* **2000**, *56*, 331.

[33] R. Sarangi, S. DeBeer George, D. Jackson Rudd, R. K. Szilagyi, X. Ribas, C. Rovira, M. Almeida, K. O. Hodgson, B. Hedman, E. I. Solomon, *J. Am. Chem. Soc.* **2007**, *129*, 2316.

[34] "Dithiolene Chemistry": *Progress in Inorganic Chemistry, Vol. 52* (Ed.: E. Stiefel), Wiley, New York, **2004**, pp. 1–681.

[35] SADABS, 2006/1, Bruker AXS Inc., Madison, WI, **2007**.

[36] ShelXTL 6.14 Bruker AXS Inc., Madison, WI, **2003**.

[37] ShelXL97, G. M. Sheldrick, University of Göttingen, Göttingen, **1997**.

[38] Orca—an ab initio, DFT and Semiempirical Electronic Structure Package, Version 2.7, Revision 0, F. Neese, Institut für Physikalische und Theoretische Chemie, Universität Bonn, Bonn, **2009**.

[39] A. D. Becke, *J. Chem. Phys.* **1986**, *84*, 4524.

[40] a) J. P. Perdew, W. Yue, *Phys. Rev. B* **1986**, *33*, 8800; b) J. P. Perdew, *Phys. Rev. B* **1986**, *33*, 8822.

[41] a) A. D. Becke, *J. Chem. Phys.* **1993**, *98*, 5648; b) C. T. Lee, W. T. Yang, R. G. Parr, *Phys. Rev. B* **1988**, *37*, 785.

[42] F. Neese, E. I. Solomon in *Magnetism: From Molecules to Materials, Vol. 4* (Eds.: J. S. Miller, M. Drillon), Wiley, New York, **2002**, p. 345.

[43] A. Schäfer, C. Huber, R. Ahlrichs, *J. Chem. Phys.* **1994**, *100*, 5829.

[44] A. Schäfer, H. Horn, R. Ahlrichs, *J. Chem. Phys.* **1992**, *97*, 2571.

[45] a) K. Eichkorn, F. Weigend, O. Treutler, R. Ahlrichs, *Theor. Chem. Acc.* **1997**, *97*, 119; b) K. Eichkorn, O. Treutler, H. Öhm, M. Häser, R. Ahlrichs, *Chem. Phys. Lett.* **1995**, *240*, 283; c) K. Eichkorn, O. Treutler, H. Öhm, M. Häser, R. Ahlrichs, *Chem. Phys. Lett.* **1995**, *242*, 652.

[46] A. P. Ginsberg, *J. Am. Chem. Soc.* **1980**, *102*, 111.

[47] L. Noodleman, C. Y. Peng, D. A. Case, J. M. Mouesca, *Coord. Chem. Rev.* **1995**, *144*, 199.

[48] B. Kirchner, F. Wennmohs, S. Ye, F. Neese, *Curr. Opin. Chem. Biol.* **2007**, *11*, 134.

[49] F. Neese, *J. Phys. Chem. Solids* **2004**, *65*, 781.

[50] Molekel, Advanced Interactive 3D-Graphics for Molecular Sciences, available under http://www.cscs.ch/molekel/.

[51] F. Neese, *Inorg. Chim. Acta* **2002**, *337*, 181.

[52] S. Sinnecker, L. D. Slep, E. Bill, F. Neese, *Inorg. Chem.* **2005**, *44*, 2245.

[53] S. DeBeer George, T. Petrenko, F. Neese, *Inorg. Chim. Acta* **2008**, *361*, 965.

[54] J. Pipek, P. G. Mezey, *J. Chem. Phys.* **1989**, *90*, 4916.

Received: December 9, 2009
Published online: March 5, 2010

